nature portfolio

https://doi.org/10.1038/s41563-022-01223-3

Supplementary information

Multiscale hierarchical structures from a nanocluster mesophase

In the format provided by the authors and unedited

Supplementary Information for

Multiscale Hierarchical Structures from a Nanocluster Mesophase

Haixiang Han[1,†], Shantanu Kallakuri[1], Yuan Yao[1], Curtis B. Williamson[2], Douglas R. Nevers[2], Benjamin H. Savitzky[3], Rachael S. Skye[1], Mengyu Xu[1], Oleksandr Voznyy[4], Julia Dshemuchadse[1], Lena F. Kourkoutis[5,6], Steven Weinstein[7], Tobias Hanrath[2*], Richard D. Robinson[1*]

[1]Department of Materials Science and Engineering, Cornell University, Ithaca, NY 14853, USA.

[2]Robert F. Smith School of Chemical and Biomolecular Engineering, Cornell University, Ithaca, NY 14853, USA.

[3]Department of Physics, Cornell University, Ithaca, NY 14853, USA.

[4]Department of Physical and Environmental Sciences, University of Toronto Scarborough, Toronto, Ontario M1C 1A4, Canada

[5]School of Applied and Engineering Physics, Cornell University, Ithaca, NY 14853 USA.

[6]Kavli Institute for Nanoscale Science, Cornell University, Ithaca, NY 14853, USA.

[7]Department of Chemical Engineering, Rochester Institute of Technology, Rochester, NY 14623, USA.

[†]Present address: School of Materials Science and Engineering, Tongji University, Shanghai, 201804, China.

*Correspondence to: th358@cornell.edu and rdr82@cornell.edu

Contents

1. Supplementary texts and figures 3
1.1 Preparation of the thin film 3
1.2 Laser diffraction: quantification of experimental data and derivation 3
1.3 Coloration of magic-sized cluster thin films from reflective diffraction and dispersion: quantification of experimental data and model 8
1.4 Dipole-dipole section 12
1.5 Formation mechanisms 13
1.6 Simplified assembly mechanism used to estimate the wavelength of deposits 15
1.7. Estimate of ridge height based on relative rates of wall solidification versus evaporation 22
1.8 Unwinding the twisting bundles of the thin film 24
1.9 Proposed mechanism for the hierarchical assembly of twisting structures 25
1.10 Optical properties of the thin film 27
1.11 Extension of hierarchical self-assembly to other nano systems 30
2. Supplementary table 65
3. References 67

1. Supplementary texts and figures

1.1 Preparation of the thin film

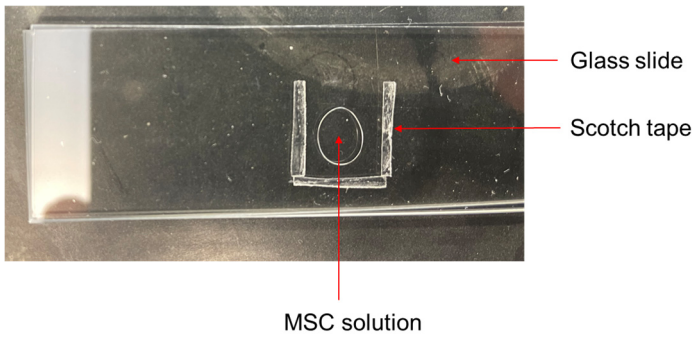

Supplementary Fig. 1. Experimental setup for the preparation of the thin film with linearly aligned fibers.

1.2 Laser diffraction: quantification of experimental data and derivation

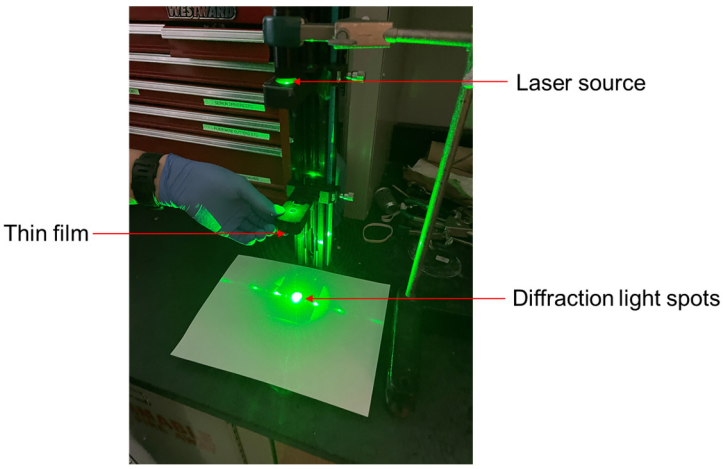

Supplementary Fig. 2. Experimental setup for the laser diffraction through the thin film.

Model of diffraction

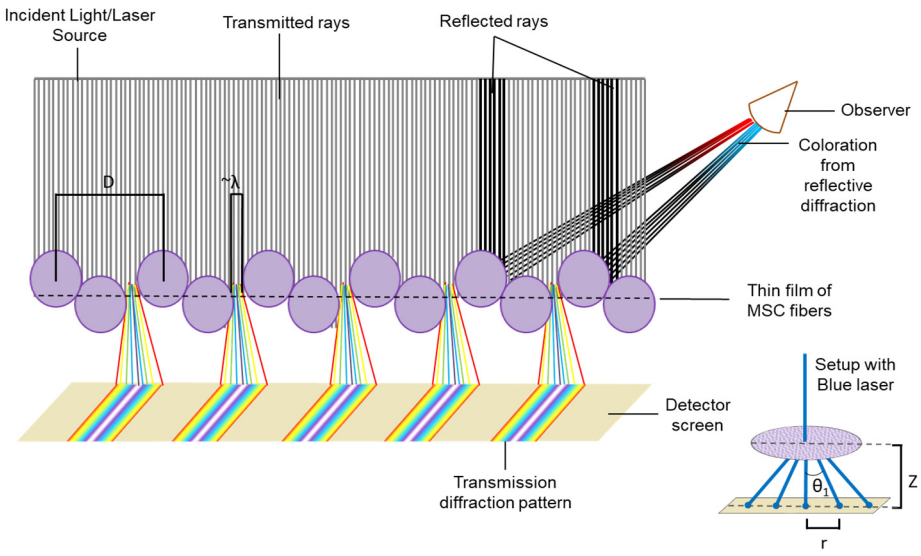

Supplementary Fig. 3. Schematic illustration of transmissive and reflective diffraction from the thin film with highly aligned fibers.

The filament layers show both transmissive diffraction and color upon reflection towards the observer originating from the incident light beam that bounces off the periodically ordered fibers as shown in **Supplementary Fig. 3**. The color depends on the path difference that this light undergoes upon reflection and then reaching the observer. By quantifying these modes, accounting for interference of the waves passing, we are thus able to accurately measure and study this platform. This data gives us additional information on the overall quality of the film as we scan across the film to identify regions of disorder, edges and grain boundaries. The transmissive diffraction pattern has been quantified and the empirical data has been used to develop a model through simulation as detailed below. For the transmission experiment, we pass a laser through our film and study the resultant diffraction patterns. We have used both violet laser of 405 nm and green laser of 532 nm wavelength with the laser's position fixed relative to the film and the distance of the film from the detector/observer fixed at 25 cm for consistency. Based on the periodic pattern seen, we know there is a diffraction grating being formed. To determine its line density we assume a grating of dimension N lines/mm being formed and calculate an effective line spacing. We see the first maxima being formed at 4.2 cm (for violet laser) and 5cm (for green laser) from the point of intersection of the thin film normal and detector screen. This

is the first order maxima of the effective grating formed by the thin film. Based on standard diffraction grating equations, we know:[1-2]

$$D\sin(\theta_k) = k\lambda$$

Where D is the slit-to-slit center-to-center spacing measured in nm/line or nm/slit as shown in **Supplementary Fig. 3**, θ_k is the angle subtended by grating central normal at kth maximum, λ is the wavelength of the laser used for the diffraction. For the 1st order maxima (k=1) that we see at a distance of 4.2 cm above the film-to-screen normal with the laser of wavelength of 405nm (violet laser used for experiment), we get

$$D = \frac{405}{\sin(\theta_1)} = \frac{405}{\sin\left(\arctan\left(\frac{r}{Z}\right)\right)} = \frac{405}{\sin\left(\arctan\left(\frac{4.2}{25}\right)\right)}$$

$$= 2444\ \frac{nm}{line}\ \text{(Effective grating spacing)}$$

$$\theta_1 = \text{Tan}^{-1}\left(\frac{r}{Z}\right) = \text{Tan}^{-1}\left(\frac{4.2}{25}\right) = 9.54^0 \text{for first maxima}$$

$$\text{Grating slit} - \text{to} - \text{slit center} - \text{to} - \text{center spacing} = 2.44\ \text{um}$$

Therefore, the distance between consecutive line centers (center-to-center distance between successive filaments) is 2444 nm. This is very close to to the center-to-center distance that we see from optical microscopy. Given the fact that we see distinct well-defined diffraction patterns, it is reasonable to say that while the slit-to-slit spacing is 2444nm, the individual slit opening between each set of fibers is on the order of 405 nm, the minimum laser wavelength at which we see diffraction. The slit spacing also lets us get a line density as:

$$\text{Grating's effective line density } \left(\frac{\text{lines}}{\text{mm}}\right) \text{is } = N = \frac{1}{D} = \frac{1\text{mm}}{D} = \frac{1\text{mm}}{2444\ \text{nm}}$$

$$= 410\frac{\text{lines}}{\text{mm}}\ \text{Grating formed}$$

Based on these empirically obtained slit opening and spacing values, we developed a computational wave-propagation model based on far-field Fraunhofer diffraction. For the analysis, a finite spot size approximation has been made based on the measured laser spot dimensions of ~0.625 microns and a far-field Fraunhofer approximation has been applied since the thin-film to detector normal distance is much larger (>20,000X) than the beam width squared to laser wavelength ratio.[3] The divergence of the laser from the source to film is assumed to be near zero since lasers are very coherent. The incident light wave has been discretized using the Huygens Fresnel principle that states that a single light source can be broken into a series of infinite point sources; in order to simplify it for finite analysis calculations using point sources spanning the illuminated area.[4] These point sources are placed at the slit-slit distance of 2444 nm from each other based on the experimental laser diffraction data we obtained earlier and validated using optical microscopy. We can now get the total diffraction intensity for the light wave transmitted through the thin-film grating. This can be done as follows: Consider an initial intensity of I_0 passing completely orthogonal to the filament grating. The multi-slit grating equation for intensity of transmitted light can then be given by the equation below:[1]

$$I(\theta) = I_0 * \left(\frac{D}{Z}\right) * \mathrm{sinc}^2\beta * \frac{\sin^2(\frac{N\delta}{2})}{\sin^2(\frac{\delta}{2})}$$

where $\delta = \frac{2\pi Dx}{\lambda Z}$, $\beta = \frac{\pi xw}{\lambda Z}$, and $I(\theta)$ is the intensity of light seen at the detector/observer. I_0 is the intensity of light source, N is the number of slits illuminated, D is the inter-slit spacing of 2444 nm based on laser diffraction and microscopy, x is the iterative position of the incident light point source in the discretized source array, λ is the wavelength of the source (405nm for the violet laser and 532 nm for the green laser used), w is the slit-aperture dimension of each slit and Z is the normal distance from the plane of the thin-film to the plane of the detector screen. θ_k is the angle subtended by the kth maximum of the emergent light transmitted through the film with the normal from the thin film plane to detector plane. Utilizing these variables and derivations, we obtain the following diffraction pattern shown in **Figure 4** (main text) for the combined grating which corresponds almost exactly with our experimental Laser diffraction data. The strong

correlation between simulation and experiment seen here allows us to conclude that our thin film acts as a transmissive grating of effective spacing 410 lines/mm with slit opening on the order of 405 nm and provides a very convenient way to quantify and study film properties and uniformity.

1.3 Coloration of magic-sized cluster thin films from reflective diffraction and dispersion: quantification of experimental data and model

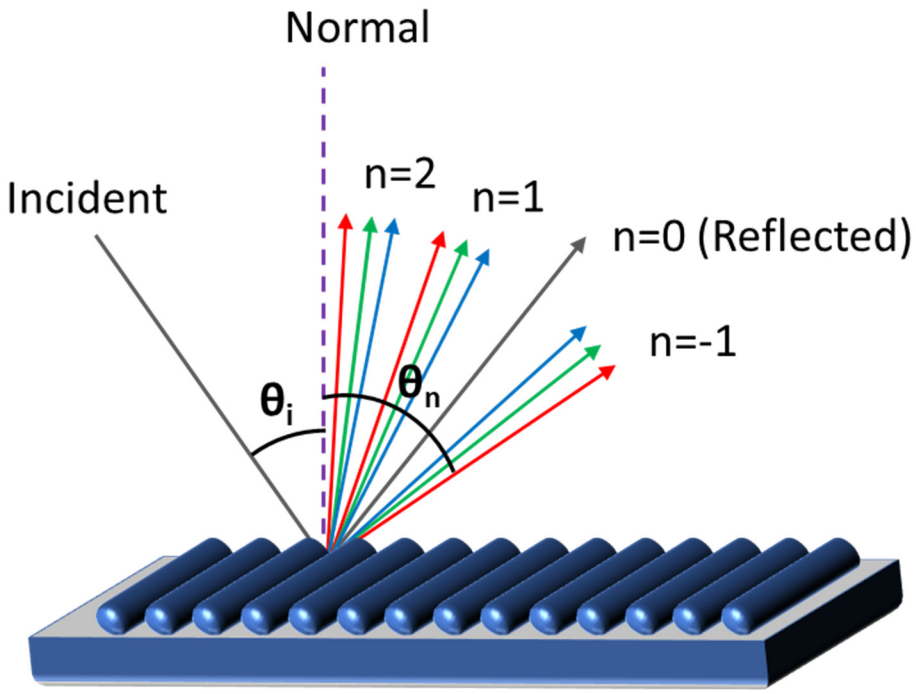

Supplementary Fig. 4. Schematic illustration of reflective diffraction and dispersion from the thin film illustrating the phenomenon of coloration

We have also quantified the colors observed on the surface of the thin film with our model of reflective diffraction and dispersion as seen below:

When light consisting of multiple colors is incident on the magic sized cluster cable bands, it behaves as a diffraction grating that reflects the incident light. The incident light is then reflected, but also diffracted according to the wavelengths of its component colors, as is seen in regular diffraction gratings and compact disc surfaces. [5-6] This dispersion allows us to observe multiple colors in the form of a rainbow when we look at the magic sized cluster thin film by eye **(Supplementary Fig. 5)**. Mathematically, this can be treated as follows:

The general diffraction grating equation can be formulated as[5]

$$n\lambda = d_G(sin\theta_i - sin\theta_n)$$

where, θ_i is the angle subtended at the grating surface normal by the light incident on the magic sized cluster bands in the thin film; θ_n is the angle subtended by the diffracted light originating from the magic sized cluster bands with the surface normal; n is the order of

diffraction being observed (typically orders 1,-1 are the most intensely visible diffracted rays); λ is the wavelength of the incident light, and d_G is the center-to-center interval distance between the periodically arranged magic sized cluster bands. Since the negative sign has been included in the equation, this means the angle of incidence is positive when subtended to the left (counter-clockwise) of the normal and the angle of diffraction is positive when subtended to the right (clockwise) of the normal.

This allows us to rearrange the equation and solve for the n^{th} order diffraction angle θ_n as :

$$\theta_n = \arcsin(sin\theta_i - \frac{n\lambda}{d_G})$$

For a 30° angle of incidence, we can calculate the angles of diffraction for -1,0,1,2 orders as seen in the table below:

For 30^0 incidence	Blue light (405 nm)	Green light (540 nm)	Red light (700 nm)
-1^{st} order (n=-1)	41.45^0	45.73^0	51.26^0
0^{th} order (n=0)	30	30	30
1^{st} order (n=1)	19.76^0	16.5^0	12.71^0
2^{nd} order (n=2)	10.14^0	3.9^0	-3.44^0

Now, since we know the -1^{st} and 1^{st} order peaks are most intense in diffraction generally, we can solve for them. Considering the first order peak, we get θ_n as 19.76°, 16.5°, 12.71°. Considering first order diffraction, this can be represented from the figure above (**Supplementary Fig. 4**) as follows below (**Supplementary Fig. 5**).

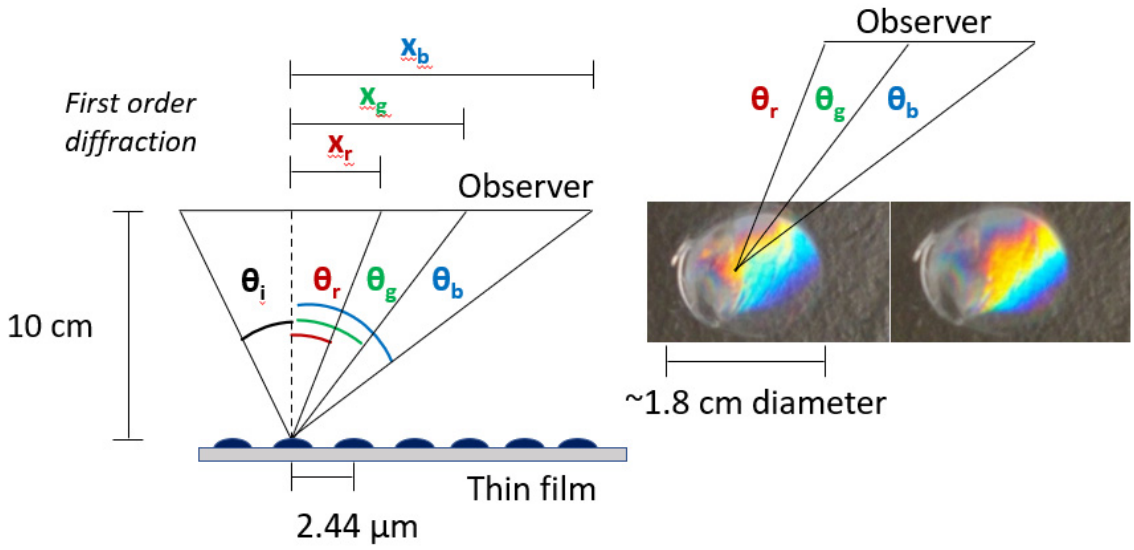

Supplementary Fig. 5. Schematic illustration of reflective diffraction and dispersion from the thin film's aligned magic sized cluster bands and an order of estimate

When we now place a glass slide with the thin film at a normal distance of 10 cm from our eyes, these angles θ_r, θ_g, θ_b, subtend spans of x_r, x_g, x_b. These distances can be calculated by simple trigonometry as follows:

$$tan\theta_r = \frac{x_r}{10}$$

$$tan\theta_g = \frac{x_g}{10}$$

$$tan\theta_b = \frac{x_b}{10}$$

When we observe the film from a 10 cm distance, this gives us values for the distances spanned from the thin film normal as :

$$x_r = 10\ tan\theta_r = 2.26\ cm$$

$$x_g = 10\ tan\theta_g = 2.96\ cm$$

$$x_b = 10\ tan\theta_b = 3.59\ cm$$

The total span subtended from red to green colors at the observer = (3.59-2.26) = 1.33 cm

As we tilt the film from left to right and change angles, we also observe the tilting change the coloration as we expect from fully blue to the rainbow spectrum and then to fully red on the other end as seen in **Supplementary Fig. 6** since we are changing the angle of incidence.

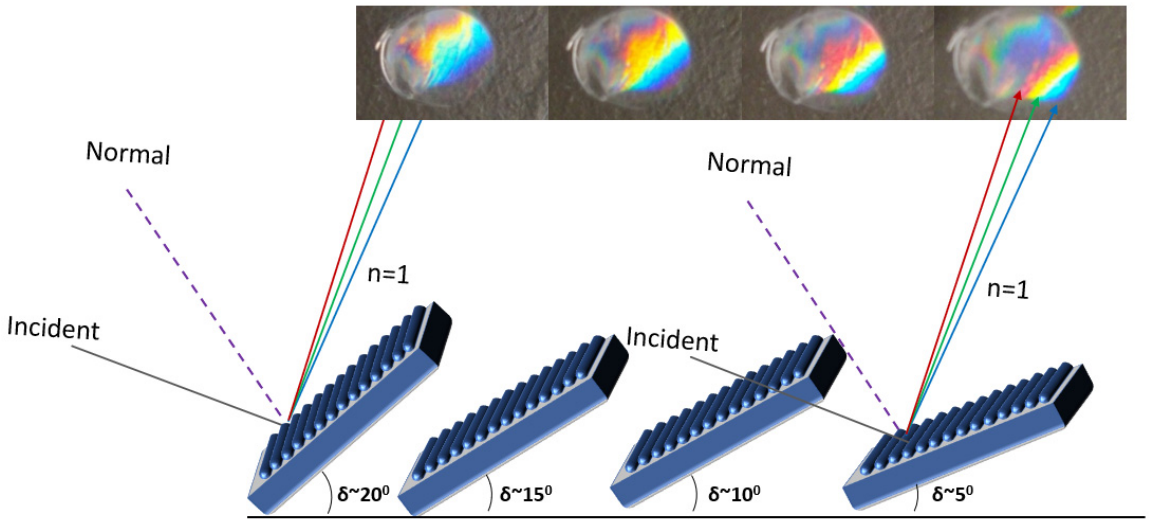

Supplementary Fig. 6. Tilt series showing the diffracted spectrum move from completely red when the glass slide containing the thin film is tilted anticlockwise from as shown in figure and transitioning to completely blue when tilted clockwise showing the sensitivity

As we observe from the figures above and the image of the colors seen in the thin film (which is ~1.8 cm in dimension here) this correlates very well with our experimental observation of ~1.33 cm and serves as additional confirmation of our model. It also provides us additional simple equipment-free ways to quantify and study the thin films made in a rapid and scalable manner and assess quality of these films.

1.4 Dipole-dipole section

The energy of interaction between two aligned dipoles is given by:[7-8]

$$E = -\frac{\mu^2}{2\pi\epsilon_o r(r^2 - d^2)}$$

Where μ is the dipole moment, ϵ_o is vacuum permittivity ($8.854 \times 10^{-12} \frac{C^2}{J \cdot m}$), r is separation distance, and d is the diameter of the nanocluster. Using a 1.5 nm diameter particle[9] with a 2.76 nm center-to-center separation (1.8 oleate ligand assumed to be not perfectly linear, 70% full length) gives values of 0.4 kJ/mol for a 7 Debye dipole moment, and 3.2 kJ/mol for a 20 Debye dipole moment.

Calculating the energy for dipole interaction from the classic formula gives a dipole attraction of 0.4 to 3.2 kJ/mol (7 D to 20 D dipole moment). These values are in the range of energies of regular molecular dipole-dipole attractions (~1.5 kJ/mol) and of the kinetic energy of linear species at RT (~2.4 kJ/mol)[7] indicating that the dipole attraction could account for a portion of the orientational forces from the inorganic component of the oleic acid-capped CdS MSCs. The London dispersion interactions in the fatty acid chains contribute an attraction force as well. For proximate MSCs the oleate ligands in the corona interact with each other, and this results in a chain structure that locks the two MSCs together (**Supplementary Fig. 11** and **Fig. 12**).[10-11] These forces are balanced by entropic interactions; distortions of the surfactant chains introduces a repulsion force to separate the nanoparticles.[12] The dipole-dipole interaction is believed as an important driving force to facilitate the self-assembly of nanoparticles. For example, upon the removal of the protective organic shell, CdTe nanocrystals can align and aggregate into nanowires through the strong dipole-dipole interactions.[7] In addition, external magnetic fields have been used to create novel self-assembly patterns in magnetic nanomaterials by controlling the magnetic dipole-diploe interaction.[13]

1.5 Formation mechanisms

The formation of banded superstructures is a relatively common, yet intriguing, observation in thin films of soft matter[14] and involves an interplay of several phenomena at different length and timescales. In the case of the MSC films at the heart of our study, the formation of the thin films involves the evaporation of the solvent, the receding motion of the meniscus across the solid substrate and the fluid shear at the liquid/solid interface. The interaction of the first two processes (solvent evaporation and meniscus movement) is central to the formation of common coffee-ring stains by stick-and-slip motion, which has also been used to explain the formation of stripes of colloidal nanoparticles[15] and nanowires.[16]

The effect of fluid shear forces, on the other hand, is the key factor explaining the formation of banded textures in sheared thin films of liquid crystals.[14, 17-22] The mechanism responsible for these structures can be described as a relax-and-recoil process which typically does not involve the movement of a meniscus across the film surface.

Chung et al. [23] recently reported a study of thin films formed from colloidal chiral macromolecules (M13 phage) under a range of processing conditions. Their work provides a beautiful example of the evolution of the processing-structure relationship from the stick-and-slip (i.e., meniscus) dominated regime to the relax-and-recoil (i.e., shear) dominated regime. The stick-and-slip mechanism dominates at low concentrations and low pull speeds and results in the formation of banded deposits separated by gaps. The relax-and-recoil regime dominates at high concentrations and results in the formation of continuous films with even more hierarchical order, such as patterns that are periodic in more than one direction, such as their helicoidal smectic structures. Whereas the physical geometries of the two fabrication approaches are different between the work by Chung et. al and the work we report here (i.e., dip-coating vs. evaporation between two parallel horizontal plates), key phenomena including solvent evaporation, movement of the meniscus, and shear forces are comparable between the two methods.

Based on the above comparison of the microstructure for the stick-and-slip and relax-and-recoil we infer that the main MSC banded structures reported in our paper (e.g., Fig. 2C-F, prepared through slow solvent evaporation of 20 mg/mL MSC solution) are formed by the stick-and-slip mechanism and the complex hierarchies (e.g., Fig. 4B,C) are formed from

the relax-and-recoil or combination of these effects. Another interesting parallel between the MSC films in our study and the M13 phage films examined by Chung et al.[23] is that both systems exhibit a relationship between formation kinetics (either pulling speed or evaporation rate) and the structure of the formed band textures.

1.6 Simplified assembly mechanism used to estimate the wavelength of deposits

The formation mechanism of the highly aligned bands is likely due to a combination of well-known phenomena.[24] The gap that confines the MSC liquid solution is 100 μm, while deposited solids of 8 μm in thickness are found on both surfaces (**Supplementary Fig. 14**). Thus, in its initial state ($t = t_0$), an air-liquid interface completely bridges the gap (main text, **Fig. 2B**, left) with a pinned contact line. At a later time (t_1), evaporation of the solvent induces a coffee-stain effect in which dispersed solids are convected through capillary fluid flow to the pinned wetting line (main text, **Fig. 2B**, middle).[25] As a result, three concentration regions arise: a bulk concentration, C_{bulk}, an increased concentration of dispersed solid near the interface, C_{inter}, and a much higher concentration of solids that continue to accumulate near the pinned contact line, C_{edge}. Due to the accumulation of solids at the edge, the evaporation rate at the center of the gap is higher than near the pinned contact line, and as a result, the interface curvature increases (main text, **Fig. 2B**, middle). The continued accumulation of solids near the wetting line leads to a phase change which is augmented by temperature change from evaporative cooling (main text, **Fig. 2B**, right; **Supplementary Fig. 17**) and cable bundles form. Convective fluid motion coupled with increased confinement of the interface near the pinned contact line orients/packs the cable bundles such that their axes are oriented along the contact line (**Supplementary Fig. 16**). In particular, any cable bundle having an axis nearly perpendicular to the contact line will have one of its ends more immobile (towards the contact line) than the other (pointing towards the bulk fluid), and this would provide a torque to rotate/align the cables. The interfacial deformation continues until the pinning condition cannot be maintained at which point the contact line undergoes the typical stick/slip motion well known in the in colloid and polymer communities.[26-27] The interface jumps to a new location downstream, reforms, and leaves behind a deposited line of cable materials. In this new location, the contact line is pinned once again along the glass, and the concentration of the MSC solution at the interface is the same everywhere (C_{inter}). The process repeats, leaving a sequence of solidified lines along both glass plates. Our proposed mechanism is consistent with an experiment/mechanism from previous literature which an air-liquid meniscus is slowly pulled downward via controlled drainage in parallel plate geometry and leads to a similar deposition pattern.[24]

The formation mechanism just described has significant complexity, and a simplified mechanistic view may be used to estimate the wavelength of the parallel bands observed in experiment (see the following sections). The estimate assumes that the menisci shown in **Figure 2B** (main text) are sections of circular arcs that are constrained to bridge the gap between the glass slides while the coffee-stain effect occurs. The contact line initially is pinned initially and with a corresponding critical receding contact angle. Solids drawn towards the contact line accumulate and form a solid ridge that roughly follows the shape of the interface. The solid region grows (stage i and ii), and the contact line is lifted from the wall (stage ii) even while the meniscus continues to pin along the growing solid. At the same time, the radius of curvature of the interface decreases through evaporation until a critical configuration is achieved—here, the radius is half of the current spacing between glass slides, which has been reduced through solid accumulation (stage ii). For times beyond this critical configuration, the contact line continues to be pinned, the radius of curvature of the interface grows (stage iii) and solid continues to accumulate under the interface. Ultimately, the radius of the interface grows until the meniscus is tangent to the wall (stage iv), the interface abruptly snaps to the original receding contact angle (see stage v), and the process repeats (stage vi). The net result is a ridge of wavelength λ, height δ_c, with glass slide spacing, H, that satisfies $\lambda/H \sim 2\sqrt{\delta_c/H}$. Consistent with the above-described mechanism, δ_c/H may be expressed as a function of the ratio of solidification to evaporation rates (see the following section of wavelength estimate); this result is qualitatively consistent with experimentally observed trends.

Experimentally, we observe that there is a critical spacing of $H \approx 20$ microns above which the height δ_c is independent of H. For a spacing much larger than this value (> 200 microns) the bands become wavy, and the assumptions of even the simple model are likely inadequate. Restricting attention to $H \approx 20$ microns, for a given observed height of $\delta_c \approx 75$ nm, the estimate yields a value of $\lambda/H \approx 0.122$, while the experimentally measured value is $\lambda/H \approx 0.125$. Considering the approximate nature of the estimate, the closeness of the experimental and predicted values of wavelength may be fortuitous—nevertheless, the fact that these ratios are the same order of magnitude suggests the estimate is reasonable.

Different stages for the formation of highly aligned bands

1) Critical times and configurations

Note that all mechanistic steps assume that vapor/liquid menisci are sections of circular arcs.

Stage (i) $t = 0$

Initial state

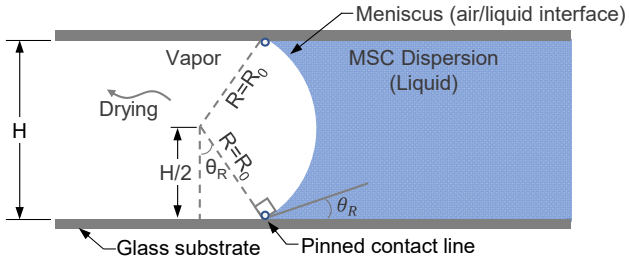

H = glass spacing

θ_R = contact angle (assumed here to be the critical receding angle for definiteness)

R = radius of meniscus

R_o= initial radius, $R_o = \frac{H}{2\cos(\theta_R)}$

In this initial configuration, the contact line is pinned and evaporation/drying of the MSC dispersion commences. The coffee stain phenomenon draws MSC solids toward the pinned contact line as shown in **Figure 2B** (main text), and phase change leads to solidification (i.e., self-assembly of MSC in a condensed phase) at the wall. As the interface sterically confines the coffee stain, the solidification roughly follows the contour of the interface and forms an approximately triangular region of solid near the wall (such as shown in stage ii). The contact line is lifted from the wall and the interface remains pinned to the growing solid (again, see stage ii). At the same time, the radius of curvature of the interface decreases as the solvent continues to evaporate. Ultimately, the configuration in stage ii is achieved.

Stage (ii) $t = t_c$

At the critical time t_c the minimum radius R=Rc is achieved.

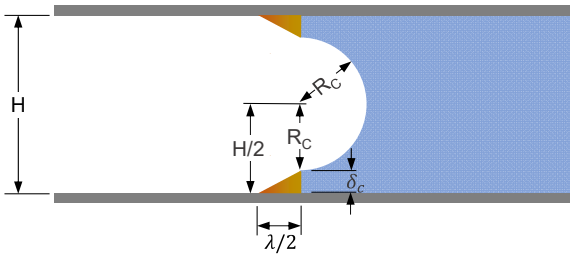

$R_c = \frac{H}{2} - \delta_c$ (by inspection)

δ_c = solids deposition height

$\frac{\lambda}{2}$ = half-width of solids deposition

At this critical time, the radius of curvature of the interface is its minimum possible value for which contact with the solid surface is maintained. This time is determined by the relative rate of evaporation (which determines the time dependent radius R) to that of solid accumulation (which determines the time dependent solid deposition height). An estimate for tc in terms of such rates is provided in the following section (2).

Stage (iii) $t_c < t < t_w$

The interface radius, R, now grows due to evaporation so that R>Rc. The coffee stain effect follows the contour of the growing interface which sterically confines the solids. As a result, the interface itself moves towards the wall and approaches a point of tangency at time t = t_w as shown in stage iv). Similarly, the thickness of the accumulated solid near the wall decreases monotonically during this time interval.

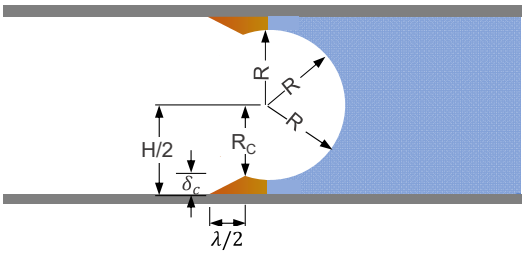

Stage (iv) $t = t_w$

At time $t = t_w$, interface is tangent to the wall, and at this point, a ridge of solid of length and height δ_c is formed completely.

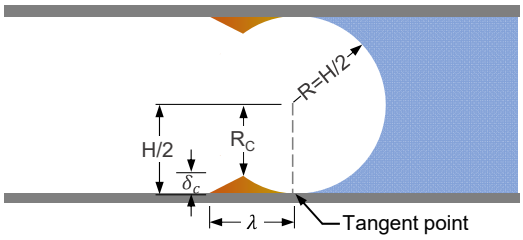

Stage (v) $t = t_w^+$

Just after the time $t = t_w$ (denoted as $t = t_w{}^+$), the interface adjusts its shape quickly after pinching off at tangent point and returns to radius R_o and contact angle θ_R. We assume negligible contact line motion after pinching off.

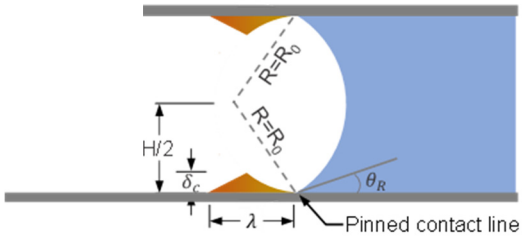

Stage (vi) The whole process i-v repeats to obtain the observed ridge pattern.

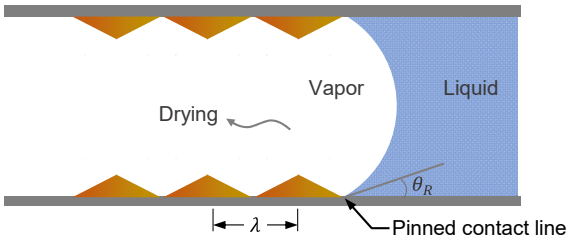

2) Wavelength Estimate

An estimate for λ is based on the tangency condition in (iii), redrawn below with more detail to facilitate analysis.

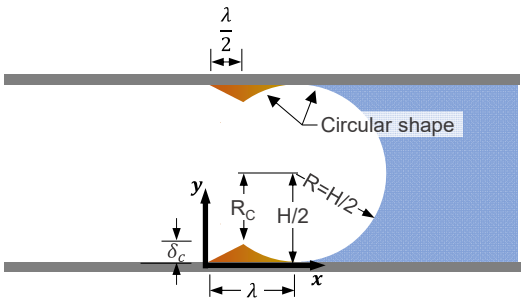

Using the coordinate system shown in the above figure, the equation of the circle satisfies the following conditions:

$$R = \frac{H}{2}, \text{ at } y = 0, x = \lambda$$

$$(x-\lambda)^2+\left(y-\frac{H}{2}\right)^2=\frac{H^2}{4}$$

Noting that the circle must pass through the location where $x=\frac{\lambda}{2},\ y=\delta_c$, the circle must satisfy

$$\left(\frac{\lambda}{2}-\lambda\right)^2+\left(\delta_c-\frac{H}{2}\right)^2=\frac{H^2}{4},$$

which can be rearranged to obtain:

$$\lambda=2\left[\frac{H^2}{4}-\left(\delta_c-\frac{H}{2}\right)^2\right]^{1/2}.$$

Upon further rearrangement, we obtain:

$$\lambda=2(\delta_c H)^{1/2}\left[1-\frac{\delta_c}{H}\right]^{1/2}$$

Making note of the fact that $\delta c/H$ is small, the binomial expansion is used to further simplify the above expression:

$$(1-x)^{1/2}\sim 1-\frac{x}{2}-\frac{x^2}{8}+O(x^3)\text{ as }x\to 0$$

and thus:

$$\lambda\approx 2(\delta_c H)^{1/2}\left[1+O\left(\frac{\delta_c}{H}\right)\right]\text{ for }\frac{\delta_c}{H}\ll 1$$

Neglecting terms of $O\left(\frac{\delta_c}{H}\right)$ and higher in the above equation and dividing by H, we arrive at the following expression for $\frac{\delta_c}{H}\ll 1$:

$$\frac{\lambda}{H}\approx 2\left(\frac{\delta_c}{H}\right)^{1/2}$$

This expression is the geometrical estimate for the relationship between spacer height, H, band period spacing, λ, and deposition thickness, δ_c.

3) Correlation of predicted to experimentally-determined values

We can compare predicted vs experimentally determined values by inserting experimentally-determined parameters (spacer height , $H = 100\,\mu m$, band period spacing, $\lambda = 2.5\,\mu m$, and deposition thickness, $\delta_c = 75\,nm$) on the left- and right-hand side of the equation:

$$\frac{\lambda}{H} = 2\left(\frac{\delta_c}{H}\right)^{1/2}$$

$$\left.\frac{\lambda}{H}\right|_{predicted} = 2\left(\frac{\delta_c}{H}\right)^{1/2} = 2\left(\frac{0.075}{100}\right)^{1/2} = 0.055$$

$$\left.\frac{\lambda}{H}\right|_{experimental} = \frac{2.5}{100} = 0.025$$

These values are within a factor of two, which is very close given the approximations used in the derivation.

An experimental observation is that there is a critical spacer thickness above which the wavelength is independent of spacer thickness. Experiments peg this value around 20 microns. Above that thickness, the ridges become wavy and other morphological effects are at play. We thus limit the application of the estimate for thicknesses to 20 micron spacer thicknesses or below.

Using the height of 20 microns in the estimate derived in section (2) we obtain:

$$\left.\frac{\lambda}{H}\right|_{predicted} = 2\left(\frac{\delta_c}{H}\right)^{1/2} = 2\left(\frac{0.075}{20}\right)^{1/2} = 0.122$$

$$\left.\frac{\lambda}{H}\right|_{experimental} = \frac{2.5}{20} = 0.125$$

Considering the approximate nature of the estimate, the closeness of the predicted and experimental values of wavelength may be viewed as fortuitous. Nevertheless, the fact that these values are the same order of magnitude suggests the estimate is reasonable. Further experiments will be needed to further test (and possibly refine, even semi-empirically) the relationship attained here.

1.7. Estimate of ridge height based on relative rates of wall solidification versus evaporation

The radius and solidification height are time-dependent quantities, $R(t)$ and $\delta(t)$.

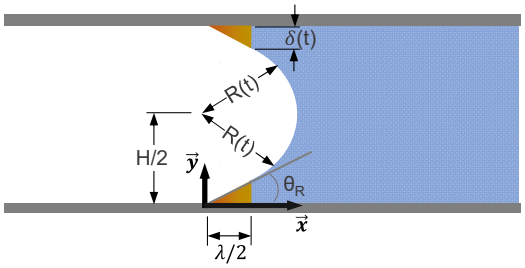

The critical configuration is limited by height δ_c and radius R_c at time t_c, as shown in stage ii of the previous section.

For t < t_c, we assume a linear relationship in time for the solid growth and radius reduction as follows:

$\delta(t) = \dot{\delta}t$, where $\dot{\delta}$ = solidification rate

$R(t) = R_o - \dot{R}t$ with $R_o = \frac{H}{2\cos\theta_R}$ (see figure i), and $\dot{R}$ = evaporation rate

$\dot{\delta}, \dot{R}$ are constants.

At the critical time $t = t_c$ (stage ii), the critical radius and solid thickness are thus expressed as

$$R(t_c) = R_c = \frac{H}{2} - \delta_c$$

$$\delta(t_c) = \dot{\delta}t_c = \delta_c.$$

and thus:

$$\frac{H}{2\cos\theta_R} - \dot{R}t_c = \frac{H}{2} - \dot{\delta}t_c$$

We now rearrange this expression to solve for t_c to obtain

$$t_c = \frac{\frac{H}{2}(sec\theta_R - 1)}{\dot{R} - \dot{\delta}}$$

So

$$\delta_c = \dot{\delta}t|_{t=t_c} = \dot{\delta}t_c = \frac{H}{2}(\sec\theta_R - 1)\frac{\frac{\dot{\delta}}{\dot{R}}}{\left(1 - \frac{\dot{\delta}}{\dot{R}}\right)}$$

and thus:

$$\frac{\delta_c}{H} = \frac{1}{2}(\sec\theta_R - 1)\frac{\frac{\dot{\delta}}{\dot{R}}}{\left(1 - \frac{\dot{\delta}}{\dot{R}}\right)}$$

The final result is, of course, dependent on the linear rate expressions assumed for $\delta(t)$ and $R(t)$, and could be refined with alternative expressions calibrated to experiment. That said, the result here indicates the importance of the relative rates of solidification and radius reduction in the creation of the wall ridges.

We note that this simplified mechanism is intended to model the patterning behavior, and does not account for more complex parameters such as the residual film thickness.

1.8 Unwinding the twisting bundles of the thin film

To illustrate the cable bundles, we immersed the high-quality periodic thin films (20 mg/mL at ~0.06 μm/s evaporation speed) into a pure hexane solution for a short time (~30 s). The hexane begins to dissolve the film and the cables start to unwind, revealing their helical twisting (**Supplementary Fig. 34 & 35**). This result shows that at higher concentrations the bands are larger, composed of more twisted cables.

1.9 Proposed mechanism for the hierarchical assembly of twisting structures

Such spontaneous self-organization processes are inherently driven by the unique structures of the constitutive subunits. The secondary structural unit in the assembly (i.e., the filament) has a branchy surface morphology with smaller filaments protruding from its circumference. These tiny, laterally protruding strands from each filament enable interactions between neighboring filaments through a combination of bonding and nonbonding interactions, such as Van der Waals force or a steric effect. To increase their stability, multiple filaments twist around each other to form a cable, and then the cables bundle and organize into bands (main text, **Fig. 4D**).[28-29] The twisted cables are nearly monodisperse when assembled into the band patterns. The thickness of this cable is a function of concentration: as we increase concentration, we increase the cable diameter. But at each concentration, there is a corresponding limit to the number of filaments within a cable; the cable diameter self-limits since the torsional stress experienced at the circumference of the cable is much larger than that at its center.[28-29] A proposed mechanism for this behavior is the balance between the strain energy of twisting and the energy reduction on assembly. Chiral subunits, such as the coiled filaments, introduce a negative term in the strain energy equation, which favors the filaments to intertwine into a twisted cable.[28] Because of the twist of the intertwined assembly, the cables exhibit a natural self-limiting growth. The filaments on the outside of the bundle strain further twist through the same angle as the filaments near the core, because the circumference they twist around is larger. At a critical radius, the energy of maintaining the cable's twist will equal the energy benefit to assembly, creating a self-limiting preferred radius for the cables. To probe whether this mechanism may be responsible for the monodispersity of the cables, we estimate the characteristic minimum radius for a twisted cable assembly to be favored. The radius of the cables is approximately 1–2 μm. The minimum radius (λ) for cable formation can be expressed as a balance between the twisting and the binding energy of the filaments as:[28]

$$\lambda = \left(\frac{d \bullet l \bullet k_B T}{\Delta E}\right)^{\frac{1}{2}}$$

where d is the separation between filaments, l is the persistence length, k_b is Boltzman's constant, T is temperature, and ΔE is the binding energy that links the filaments together,

here considered to be interactions between the neighboring filaments. The first two parameters, d and l, can be estimated from microscopy images, and we find them to be on the order of 2 nm and 2 μm, respectively. The binding energy cannot be directly measured for the MSC mesophase, but we can estimate a range based on the strength of common intermolecular interactions. Setting an upper boundary, strong ionic interactions between filaments for certain known systems are on the order of about 10 k_BT,[28] and a lower bound can be estimated for van der Waals forces of small organic molecules at around 0.05 k_BT.[30] These values yield a range of 0.02 to 0.3 μm that marks the minimum radius value for cables, which is indeed smaller than the observed cables (radius of 0.5 to 1.0 μm). The equilibrium cable size will depend on the surface energy for a specific solvent and MSC concentration and is therefore harder to accurately calculate. The effect of strain limitations on the cable radius is consistent with experimental observations, which indicates that this mechanism may be responsible for the monodispersity of the cables.

1.10 Optical properties of the thin film

In light of the unique optical properties of isolated MSC building blocks, examining the emergent optical properties in hierarchical assemblies presents intriguing scientific questions. Herein, we focus on the linearly aligned bands in thin films prepared from 20 mg/mL MSC solution whose structure and patterning behavior have been established (main text, **Fig. 3**). We have previously reported that the constituent 1.5 nm CdS MSCs have two atomic structural isomer configurations, the α- and β-phases, that have distinct characteristic absorption peaks at 324 and 313 nm, respectively.[31] The chemically induced isomerization between the phases is reversibly controlled through ad/de-sorption of alcohol molecules. The ensemble films have a shiftable absorption peak, show well-behaved diffraction grating effects, and have both linear and circular dichroism (see SI2 for more details). Moreover, the thin films formed from α-CdS MSCs have an absorption profile similar to that of the diluted solution, indicating that the hierarchical self-organization of MSCs into the band assemblies does not affect the electronic structure of the individual nanoclusters. Upon treating the thin film with methanol vapor for 30 minutes, the characteristic absorption peak changes to 313 nm, indicating a complete conversion to β-CdS MSCs. Upon removal of methanol by gentle heating, the β-phase reverts back to the initial α-phase; this conversion is repeatable over multiple cycles (**Fig. 5A,B** and **supplementary Fig. 37**). The surface patterning of the thin film does not change during the isomerization process. This endows the thin film with unique optical characteristics that may be exploited in electro-optical or sensing devices.

The band patterning in the thin films displays exceptional long-range periodicity, with the material acting as both a transmissive and reflective grating. Exposing the thin films to green ($\lambda = 532$ nm) and blue ($\lambda = 405$ nm) laser beams creates a classical diffraction pattern with a series of spots perpendicular to the alignment of the cables (**Fig. 5C and supplementary Fig. 2**). The spots are discrete without diffuse rings or blurring and are invariant regardless of the region sampled (**supplementary Fig. 9**), confirming the high level of periodicity from the grating formed by the cables. The geometry of the setup and the spacing of the peaks is consistent with the 2.5 μm spacing found by the other characterization methods; since the grating can diffract blue-light, the corresponding effective slit size is on the order of ~400 nm (**Fig. 5D**). Similarly, we observe a color

spectrum from reflected light that confirms the uniform periodicity of the striations. The bullseye patterns create a reflective grating effect similar to that seen in compact discs (**supplementary Fig. 20**).

Beyond the well-defined diffraction, the highly aligned thin films possess linear dichroism as expected, and circular dichroism, which was unexpected. The CdS MSCs have an anisotropic morphology that results in polarization anisotropy (a preferential emission direction)[32]. The anisotropy likely occurs along the long axis of the nanocluster. The interaction between nanomaterials and light will be more intense in a direction aligned with this anisotropy. Linear dichroism (LD) spectroscopy of the thin film with vertically aligned stripes provides a strong LD response, indicating highly linear optical properties (**Fig. 5E**, red plot). Upon a 90° rotation, the LD spectrum inverts, becoming a mirror image of the 0° spectrum (**Fig. 5E**, blue plot). Linear alignment of the oleic acid affects these spectra: signals in the LD spectra have a high correlation with the UV-vis absorption spectrum (**Fig. 5E**, black dashed plot at bottom) for oleic acid for wavelengths lower than 250 nm. Because the CdS MSCs do not absorb light at wavelengths longer than 350 nm, the thin film has wavelength-independent LD activity in the long wavelength region (> 350 nm), indicating that it could act as a ruled transmission grating at these wavelengths. In addition, the thin film exhibits strong CD response (**Fig. 5F**) with the two strongest CD signals appearing at 319 and 328 nm, the values of which are bisected by the MSC exitonic peak at 324 nm. As the wavelength decreases, a clear bisignate curve (change of sign within a band) is apparent: the CD signal first decreases to a negative minimum (329 nm, -376 mdeg) and then increases, passing through a zero point (324 nm), and finally reaching a positive maximum (317 nm, 226 mdeg). The bisignate spectrum shown in the CD data can be interpreted in terms of a coupled oscillator theory (exciton coupling). Exciton coupling occurs when multiple chromophores are located in close spatial proximity and the electronic excitation becomes delocalized over the entire chromophore array. To form a characteristic bisignate spectrum the chromophores must be identical (same-handedness). The change from a negative to a positive CD response can arise from the relative orientation of the chromophores and also from different chiralities. Therefore, determination of the significance of the couplet shown in the data is not straightforward and will require more extensive investigations. By simultaneously recording the absorption

spectrum, we can calculate the g-factor, which represents the CD strength of the chiral sample (**Fig. 5F**). Owing to the high intensity of the CD signal, the corresponding g-factor plot displays a similar profile as the CD response, with the maximum and minimum values appearing at 317 nm (0.007) and 329 nm (-0.011), respectively. It is important to note that a strong LD signal occurs in the same region as the CD, which could influence the strength of the CD spectrum. The Cotton effect is commonly a sign of helical structure, such as for the secondary structure α-helix of proteins.[33-34] The optical images do show helical features along the cable axis with an average pitch distance of 2.0 μm (**Fig. 5G**). One of the interesting outstanding questions in the field of chiroptic materials is: at what length scale does the asymmetry begin and how does chirality at one length scale get translated across different length scales?[35] Our optical images show that the fibers wrap into helical twists when forming the bands (**supplementary Fig. 34 and 39**). Determining the fundamental building blocks of our asymmetry, and how that block creates asymmetry through the hierarchical length scales is a subject of future investigation.

1.11 Extension of hierarchical self-assembly to other nano systems

The ability for self-assembly extends beyond the CdS MSC system. We have also investigated this assembly in oleic acid-capped CdO nanoclusters (see **SI**). Viscous, high concentration solutions of the CdO nanoclusters contain filaments (**Supplementary Fig. 39a**), the constituent building blocks for larger band structures. Controlled evaporation through identical methods as the CdS MSCs result in periodic band patterns (**Supplementary Fig. 39b**) with spacing on the same order as that observed in the CdS patterns. Higher magnifications reveals that each band is composed of two filaments that twist around with each other like DNA, again, similar to that observed in CdS MSC system (**Supplementary Fig. 33-35**). Mechanistically, these results elucidate the key role of 'softness' of the colloidal particle (parametrized by the ligand/core size ratio) to moderate the molecular level interactions that give rise to the hierarchical assembly behavior. Nanoclusters (< 2nm) have a high fraction of organic material leading to 'soft' inter-particle interactions. Colloids larger than nanoclusters (> 2 nm) have reduced soft interactions, and this diminishes their ability to assemble in hierarchical structures. To underscore the size-dependence or the assembly behavior as a function of ligand-core ratio, we have examined different core sizes for a fixed ligand length (oleate, ~18 Å). Small cores (e.g., CdS MSCs) assemble into complex structures, as shown here. Larger cores (4 nm) exhibit similar assembly characteristics, but the structures are not as well defined (**Supplementary Fig. 40**). For core sizes >4 nm, the interaction between the inorganic cores dominates and the particle 'softness' drives the formation of bcc (soft) and ultimately fcc (harder) assemblies.[36]

Extending this understanding of softness as determined by the ligand/core size ratio, we believe nanoclusters, with their large ligand shells, sit at an intermediate size range and because of this, are able to form the types of patterned hierarchical structures we show here, which are distinct. In contrast, smaller molecular systems have a different phase behavior, and are able to form structures such as micelles and lamellar assemblies, while larger systems are governed by different inter-particle 'hard' forces, forming assemblies such as bcc and fcc.

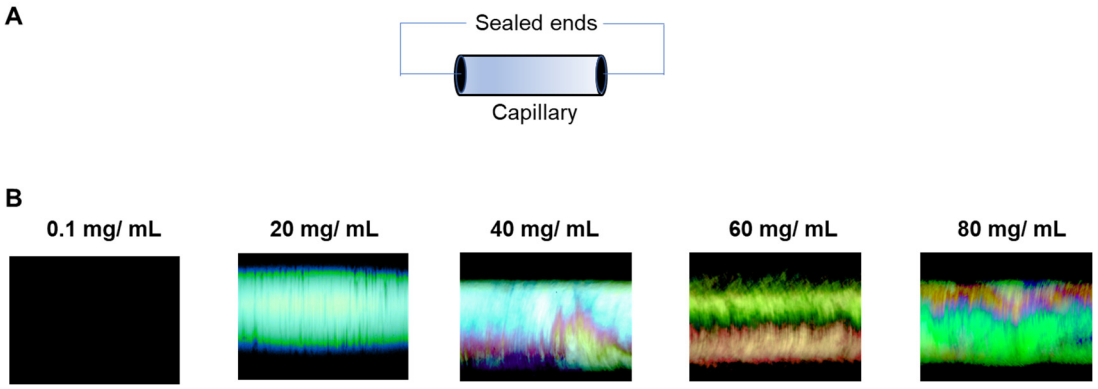

Supplementary Fig. 7. (A) Schematic illustrating the sample preparation of MSC solutions in a sealed capillary tube for polarizing microscope microscopy. (B) Polarizing microscope imagines for the MSC solutions with different concentrations. At low concentration of 0.1 mg/mL, the MSC solution does not display obvious texture, indicating the lack of long-range ordered structure, while birefringent texture starts to appear when the concentration is higher than 20 mg/mL and phase change takes place upon changing the concentration. This suggests the MSC solution has a lyotropic liquid crystal behavior which demonstrates concentration-dependent phase diagram. Note: arbitrary colors were used to clearly display the phase differences.

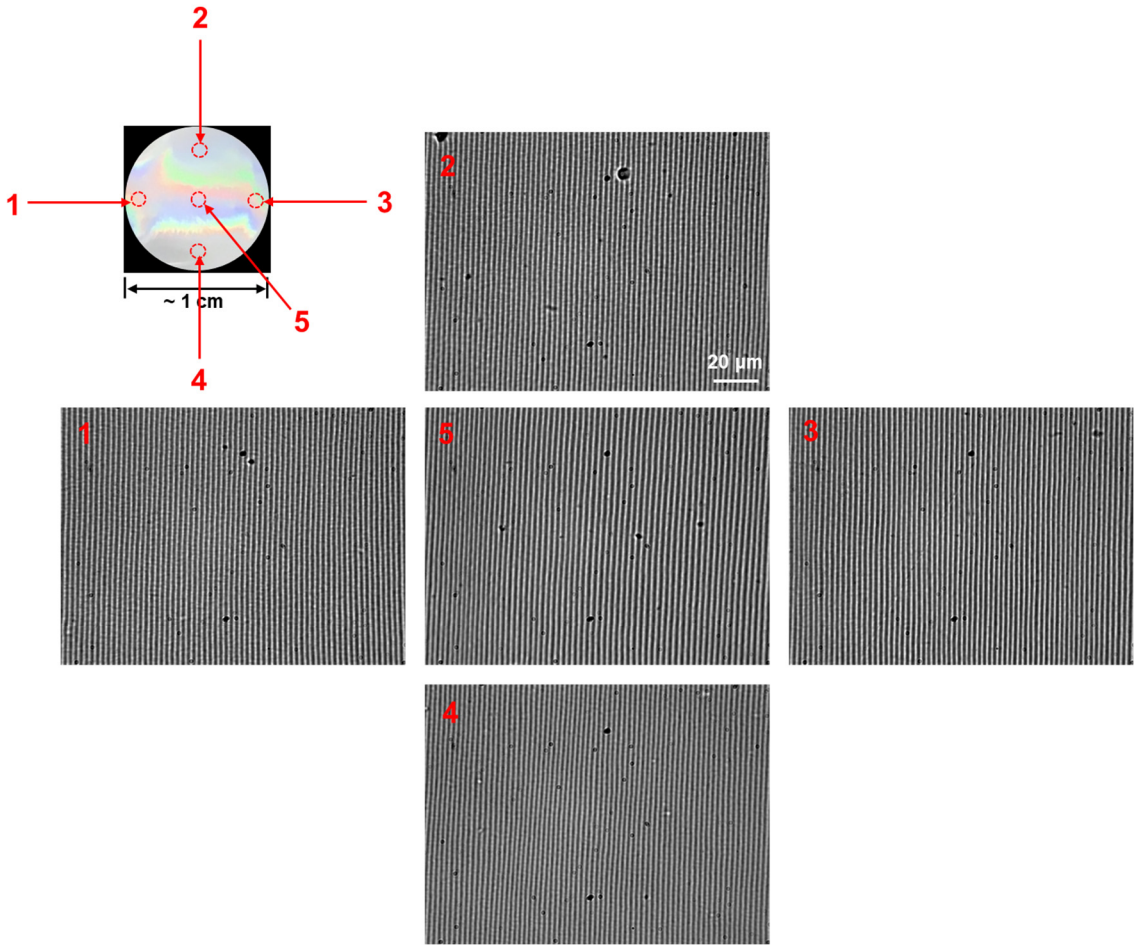

Supplementary Fig. 8. Optical microscope images for the different regions on the linearly aligned thin film. The thin film has surface periodicity at centimeter scale, which is confirmed by checking several representative regions (top left, circled with red lines). All regions demonstrate similar texture features with the same orientation and spacing.

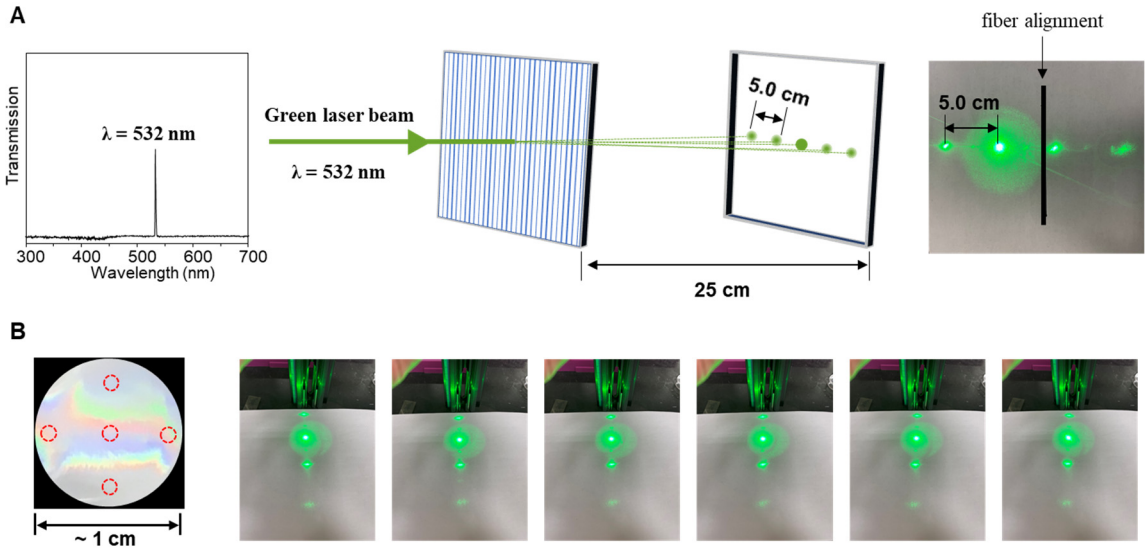

Supplementary Fig. 9. (A) Experimental setup for the laser diffraction on the thin film. The green laser beam has a characteristic wavelength of 532 nm. Through the thin film, the laser beam is diffracted into linearly aligned spots, which is perpendicular to the alignment of fibers. Depending on the distances between the thin film and the detector, and the spacing of the fibers, the averaged distance between the neighboring diffracted light spots is about 5.0 cm. (B) Inspection of different regions of the thin film by laser diffraction. All regions show similar laser diffraction patterns with respect to the orientation and distance between the light spots, confirming the homogeneity of the thin film.

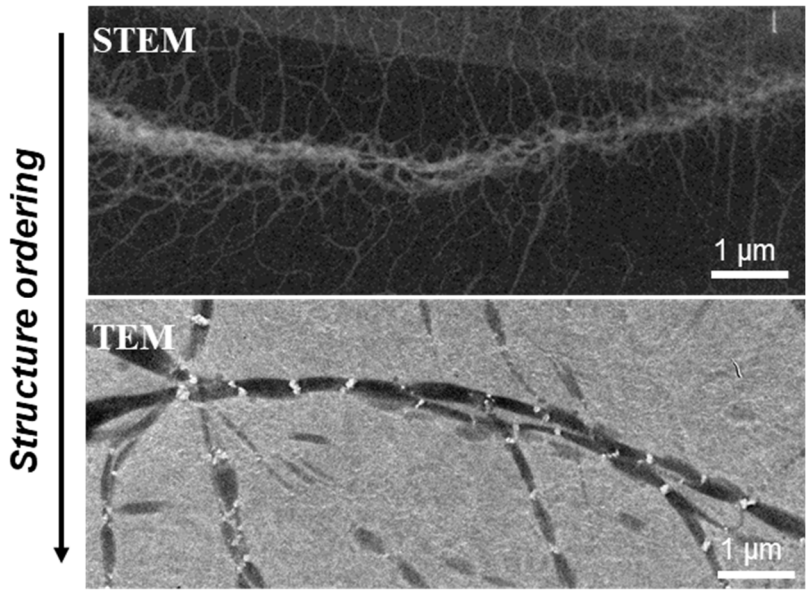

Supplementary Fig. 10. STEM image for the branchy filaments (top) and TEM image for the twisting ribbons (bottom) evolved from branchy filaments through structure ordering.

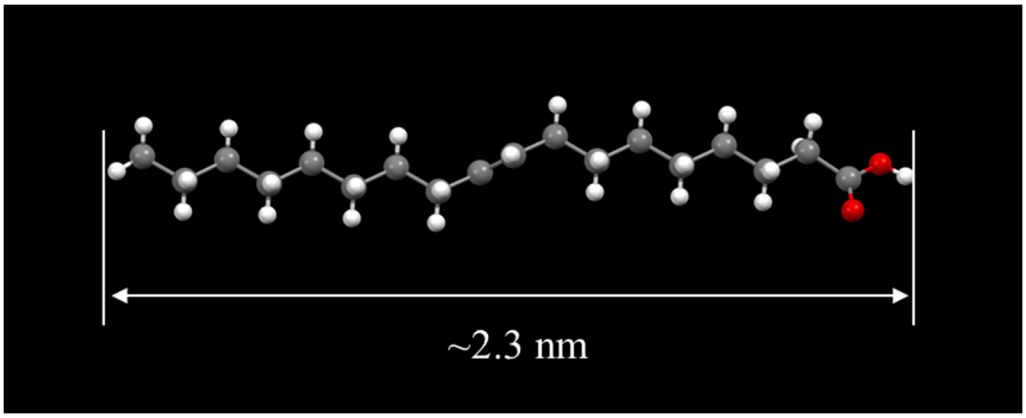

Supplementary Fig. 11. Solid state structure of oleic acid molecule.

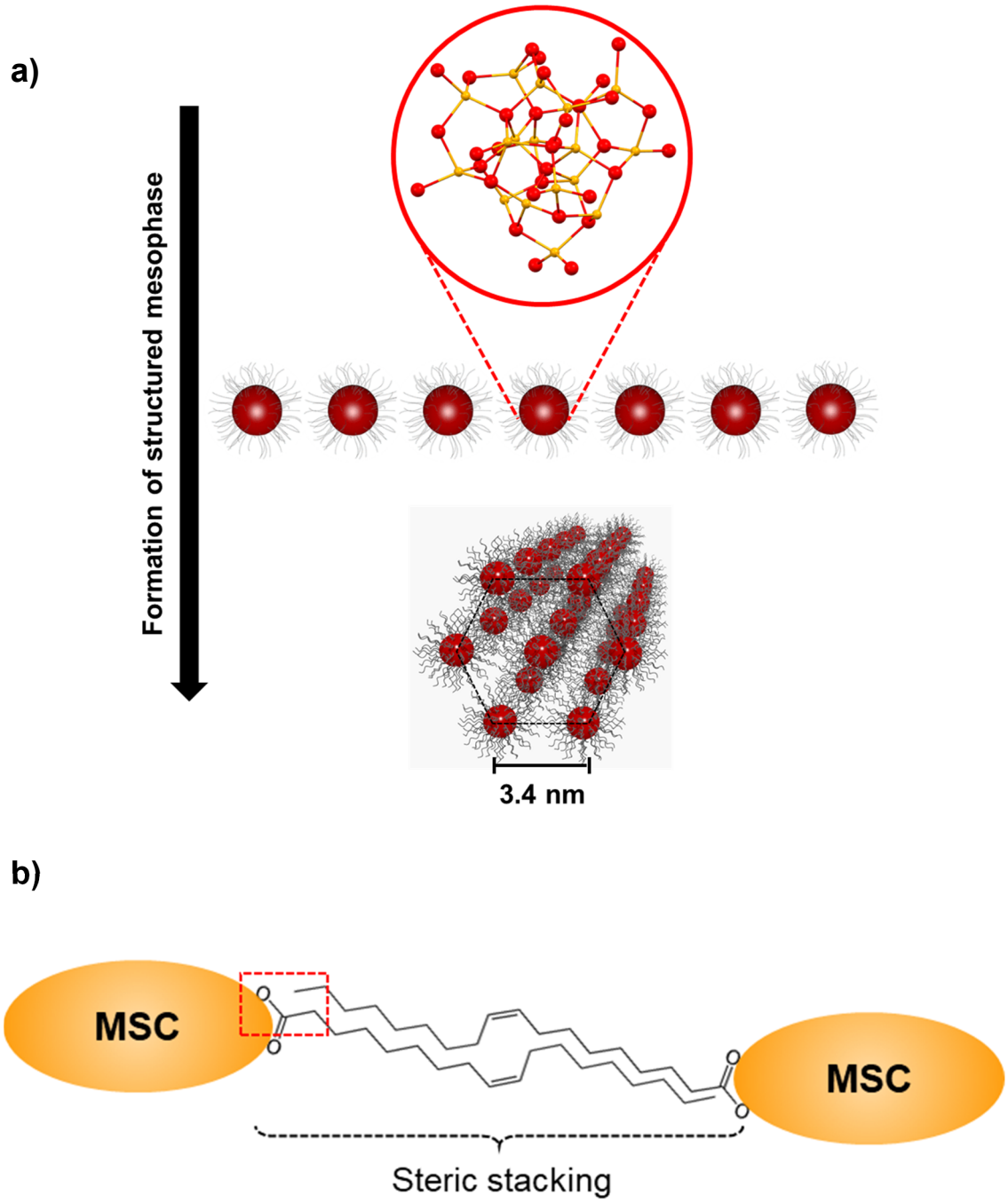

Supplementary Fig. 12. Schematic illustrating the formation of mesophase structure with a hexagonal geometry revealed by SAXS analysis (a) and the ligand-ligand interaction that links the MSCs together. Note: only representative ligands on each MSC are shown (b).

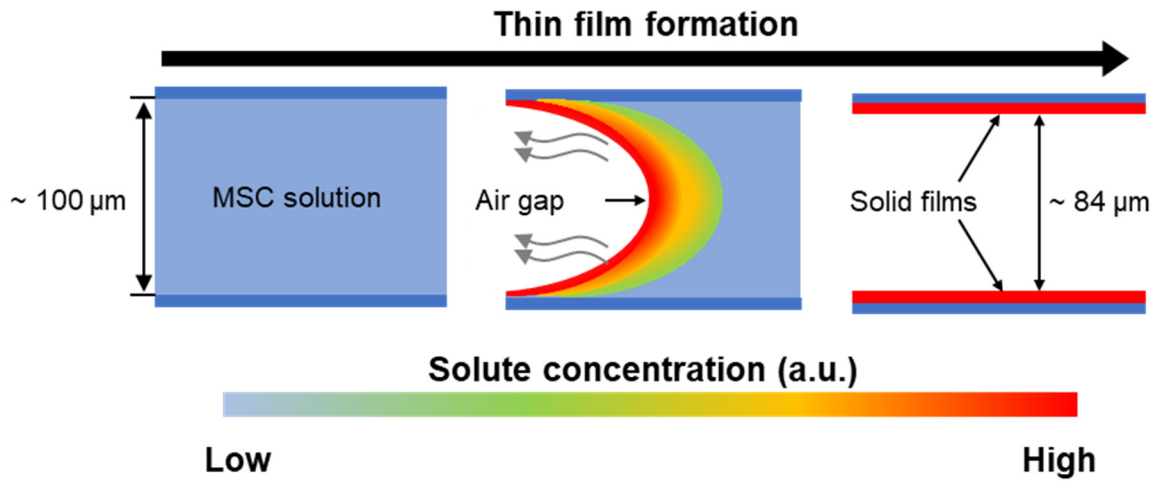

Supplementary Fig. 13. Schematic illustration of the formation of thin film deposited on the inner walls of the two glass slides. Initially, about 30 µL MSC solution (20 mg/mL in hexane) is added into the gap of two glass slides with an about 100 µm gap to confine the evaporation process. Upon solvent evaporation, a meniscus forms and the solutes start to accumulate and deposit onto the surfaces of the two glass slides. Finally, two almost identical dry thin films can be obtained, leaving a gap (about 84 µm) in between of the confining glass slides. Note that the proposed mechanism is supported by an analogous mechanism proposed to explain observations in which a colloidal suspension is drawn upwards from a pool via capillarity between vertical parallel glass plates having a 1 mm gap; the pool height is slowly lowered until slow interface motion is observed in the between the plates.[37] The ambient air is carefully controlled as well. A repetitive line pattern of colloid deposition is observed consistent with the mechanism described above. However, in the current study, evaporation provides the interface motion, the gap spacing is 10× smaller which tends to keep evaporation rates low, and phase change/fiber bundle formation is a key attribute (**Supplementary Fig. 17**).

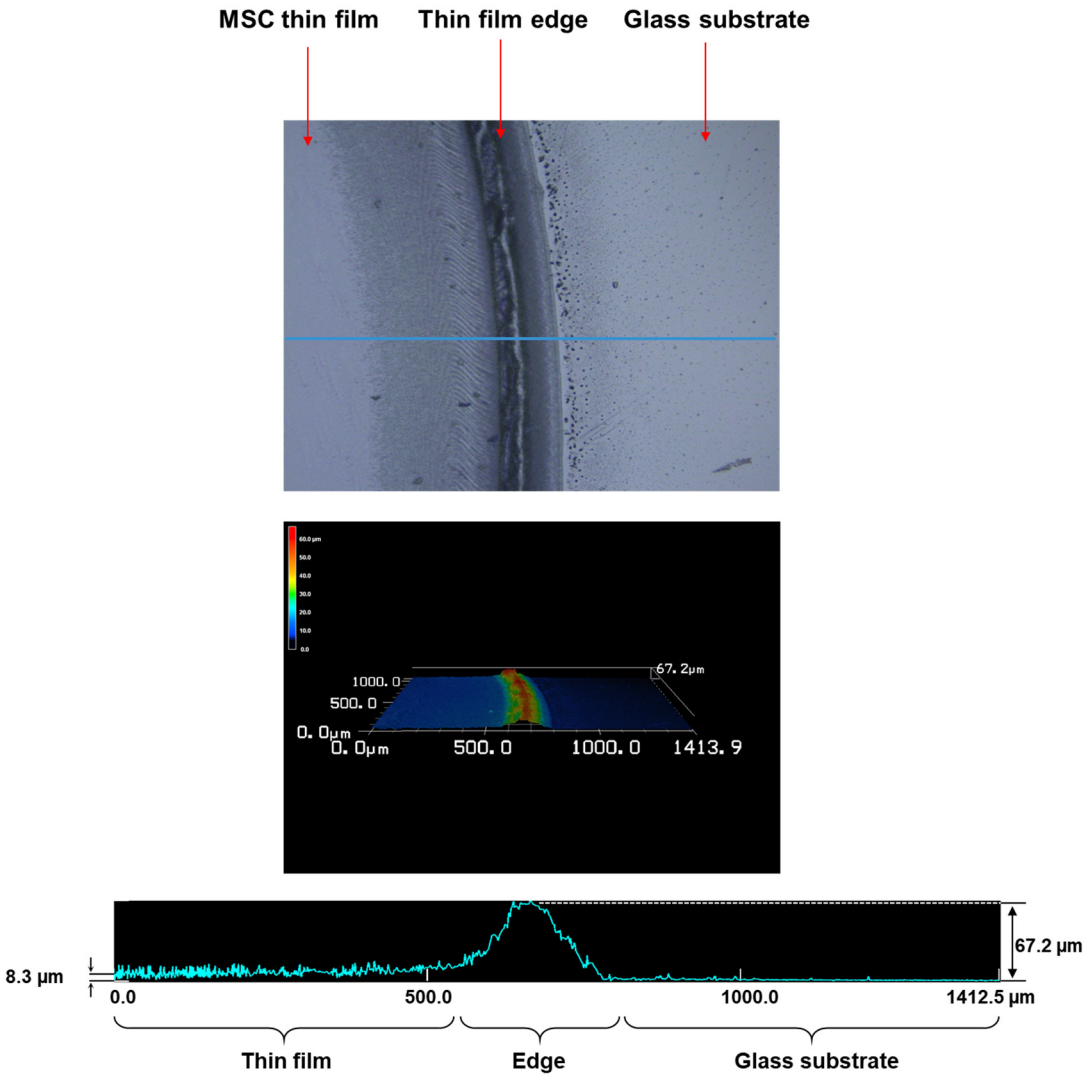

Supplementary Fig. 14. Laser scanning confocal microscopy of the edge area on the thin film. The thickness of the thin film is measured as 8.3 µm. After solvent evaporation, there is a dense boundary along the perimeter, which is formed from the "coffee-ring" effect. In this process, the liquid evaporating from the edge is replenished by liquid from the interior through capillary flow, and accompanying this flow is mass transport of MSC filaments from the center to the edge.[25] In this particular system, the capillary flow effect is not significant since the large size of the fibers exceeds the capability for capillary flow and the evaporation is not unidirectional. Both thin films on top and bottom glass slides show the similar thickness.

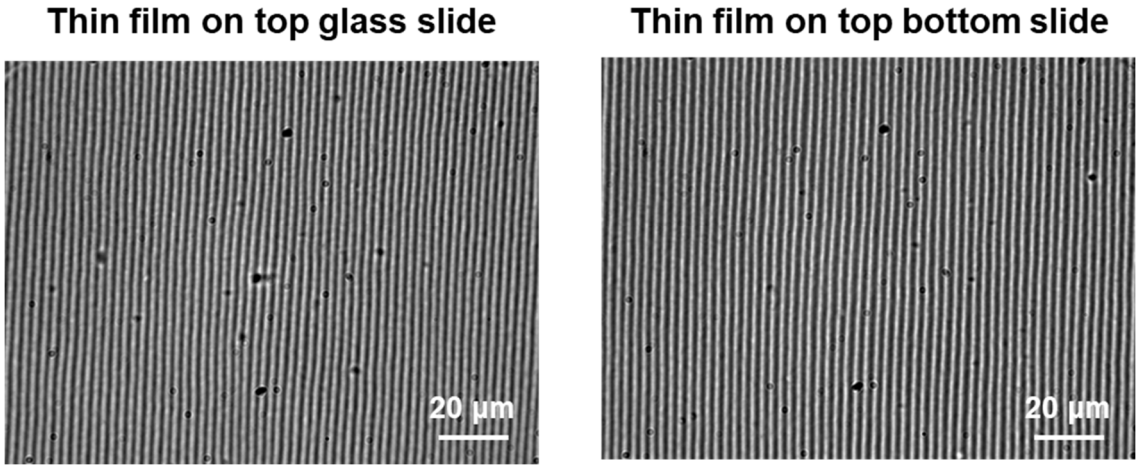

Supplementary Fig. 15. Optical microscope images for the thin films produced from top and bottom glass slides. Through the solvent evaporation method, thin films can form on both top and bottoms glass slides simultaneously and they demonstrate the same surface texture and thickness.

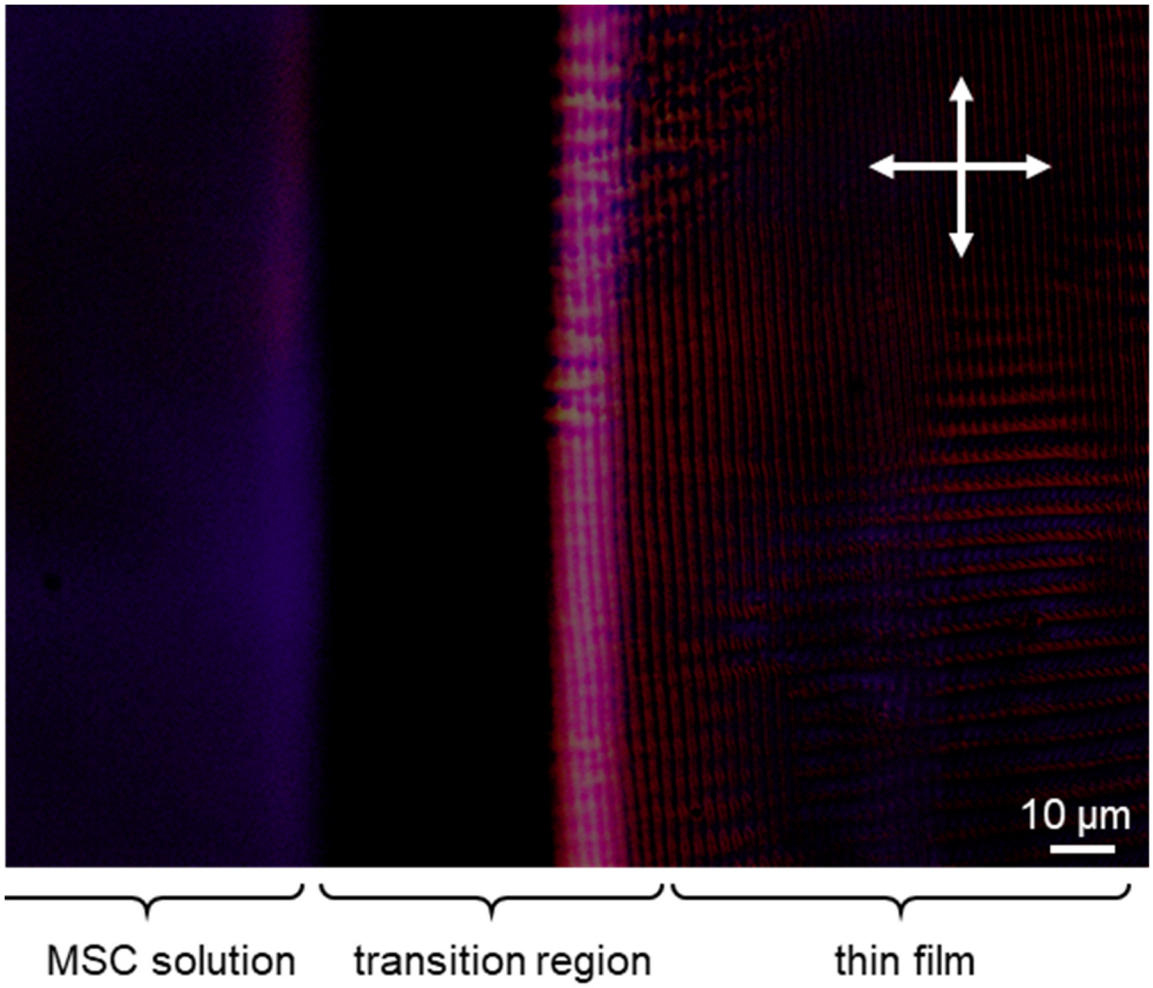

Supplementary Fig. 16. In-situ polarizing optical microscope image for the formation of highly aligned thin film upon solvent evaporation from 20 mg/mL MSC solution. Arbitrary colors are used here to clearly show the thin film formation. Under polarizing microscope, the MSC solution displays weak birefringence. During the solvent evaporation process, the drying front represents a region with high concentration contrast which make it opaque to the crossed polarized lights. The as-formed dry thin film contains fibers orientating parallelly to the evaporation front.

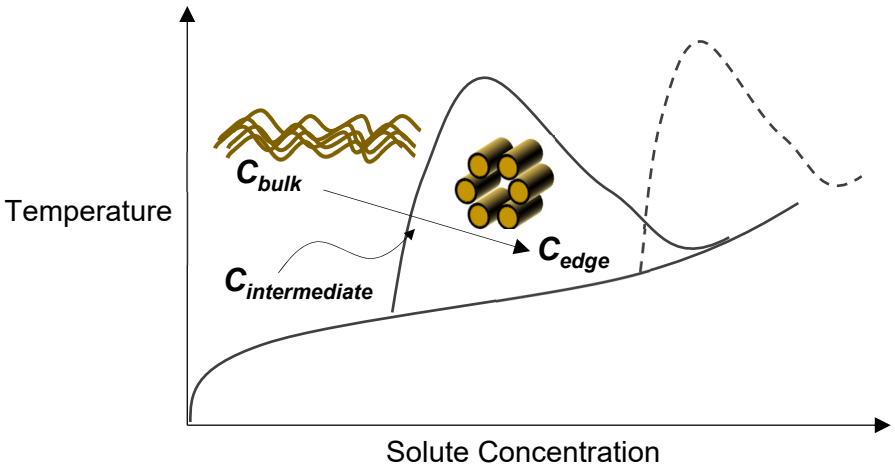

Supplementary Fig. 17. Concentration-dependent phase diagram of the MSC solution. During the film deposition process, as we move from the bulk fluid inside of the meniscus to the dried film outside the meniscus edge we observe a phase transition from a disordered set of filaments into an ordered fiber that forms the thin film through periodic condensation.

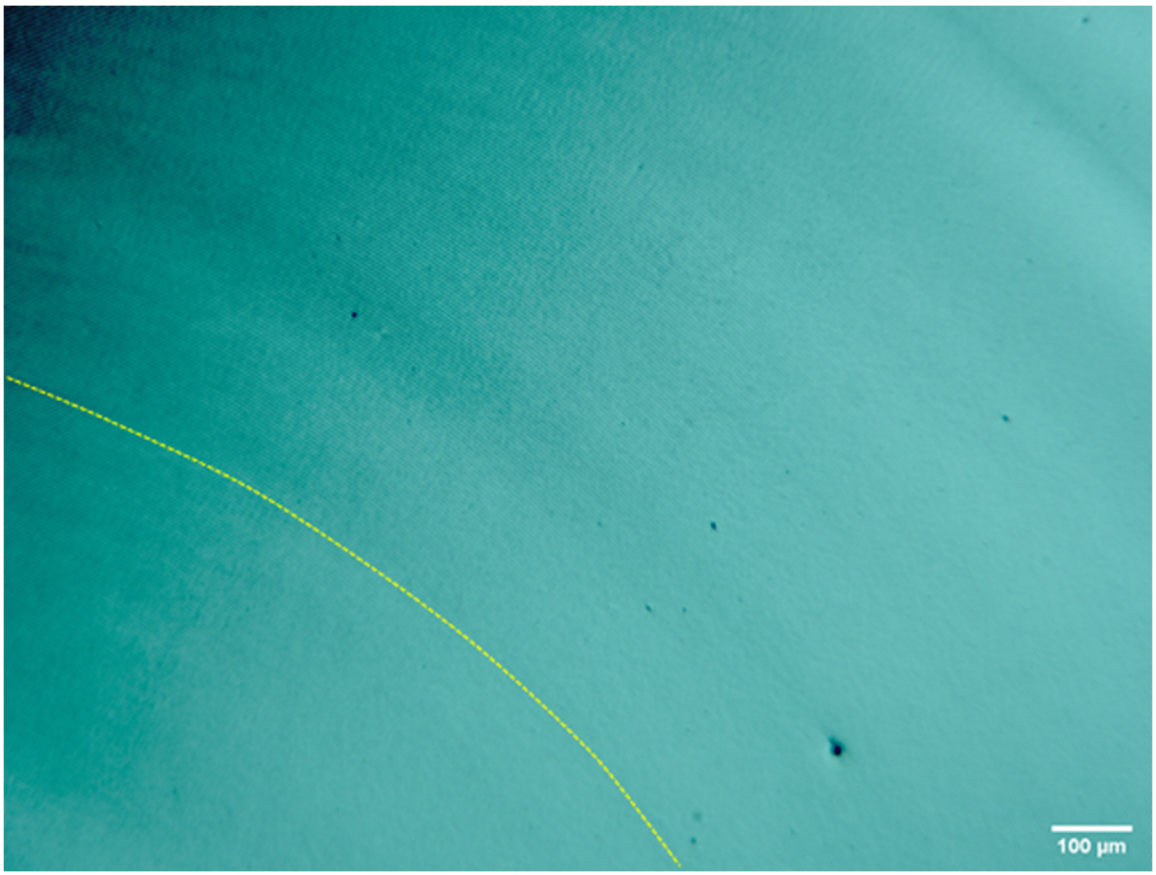

Supplementary Fig. 18. Optical microscope image of the circular thin film. The film is of nearly identical spacing as the linearly ordered film and both films show strong transmissive and reflective diffraction effects.

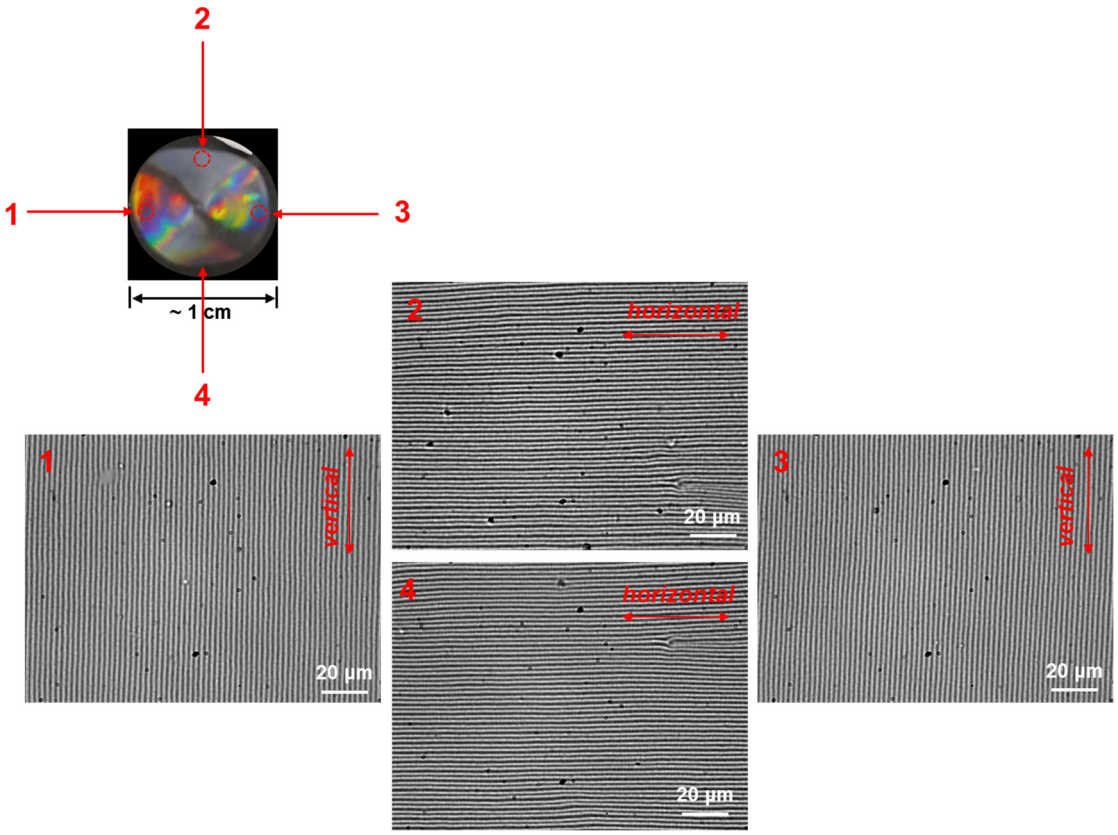

Supplementary Fig. 19. Optical microscope images for the different regions on the circularly aligned thin film. The thin film has surface periodicity at centimeter scale, which is confirmed by checking several representative regions (top left, circled with red lines). All regions demonstrate similar texture features with the same periodicity, but different orientation, which are consistent with the circular alignment of the fibers.

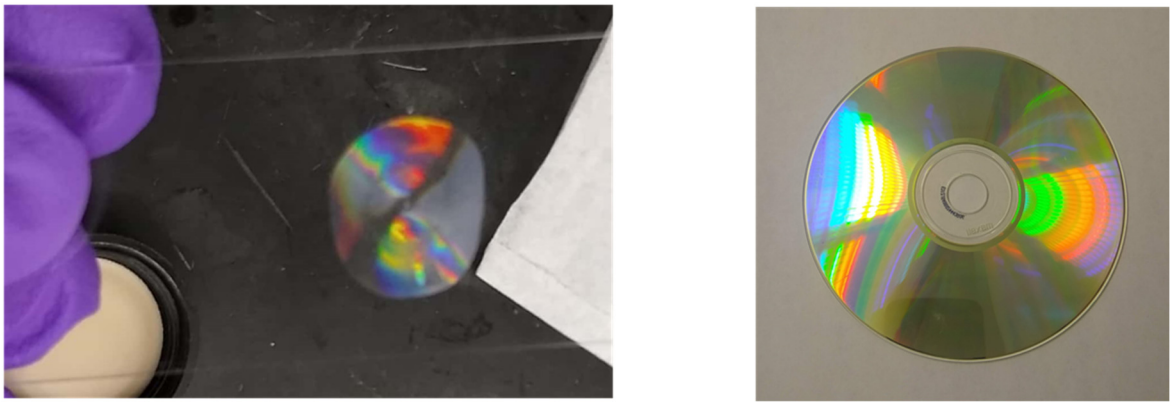

Supplementary Fig. 20. Photographs of the thin film with fibers aligned in a ring-like arrangement (left) and a real compact disc (right). The thin film reflects visible light into rainbow colors like ths CD which is also a diffraction grating reflecting on the order of visible light and near-UV wavelengths.

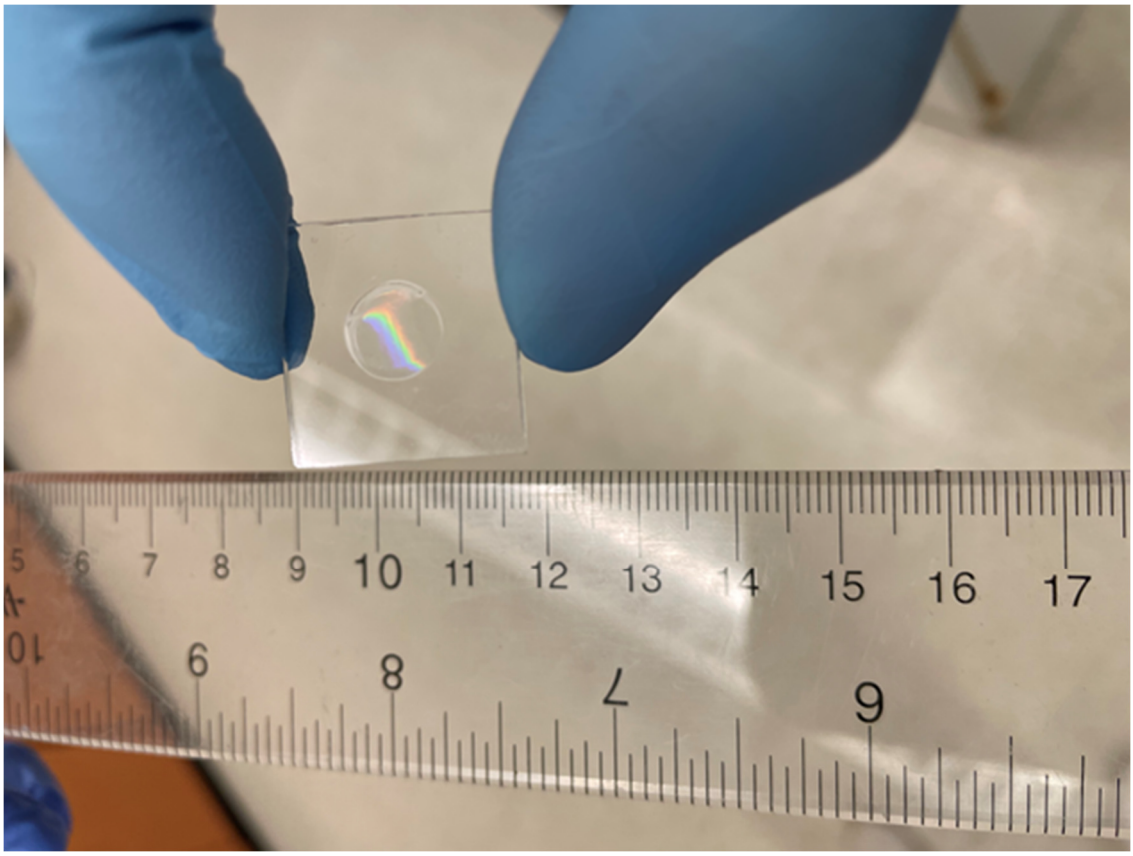

Supplementary Fig. 21. Photograph of the thin film with the linearly aligned fibers. The thin film reflects visible light into rainbow colors in a linear alignment.

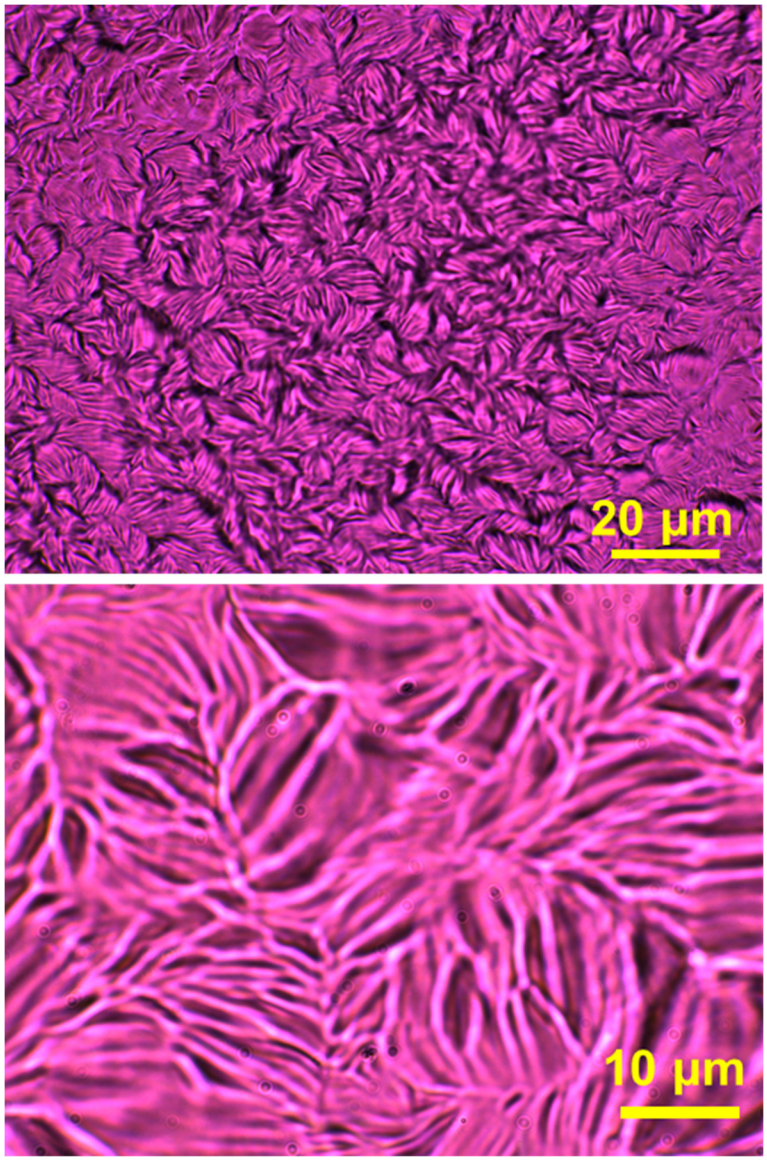

Supplementary Fig. 22. Optical microscope images of the thin films composing randomly orientated fibers. Note: arbitrary color is used in the optical microscope images.

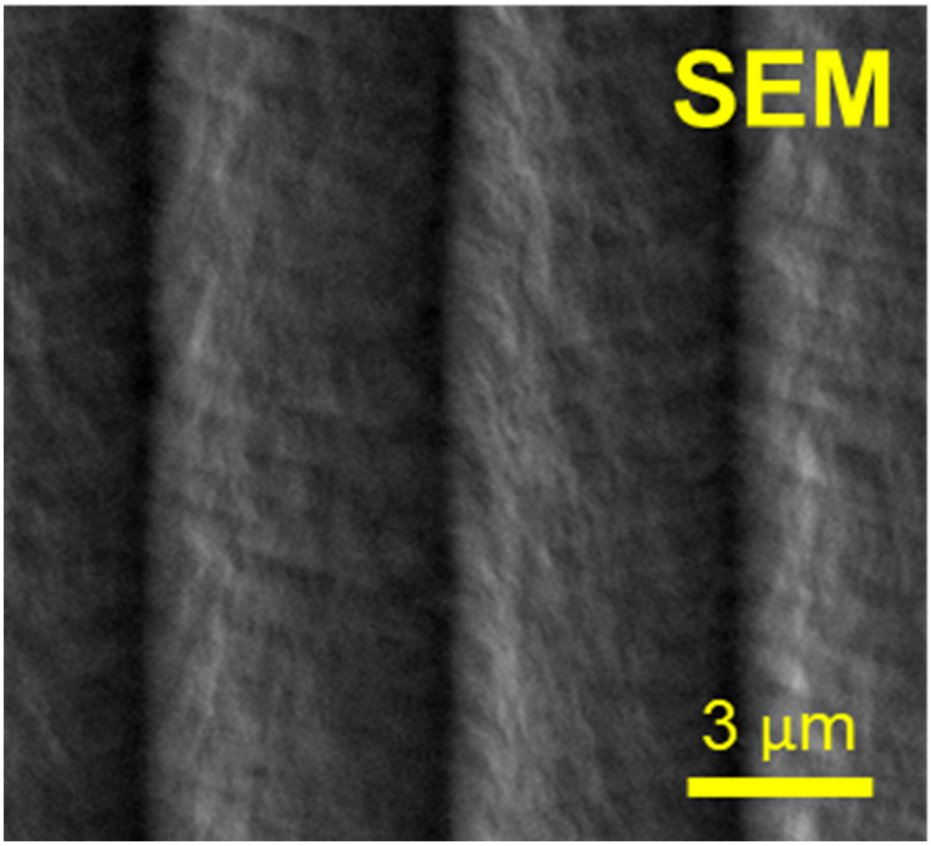

Supplementary Fig. 23. SEM images of the thin film showing fine structure in the assembled bands.

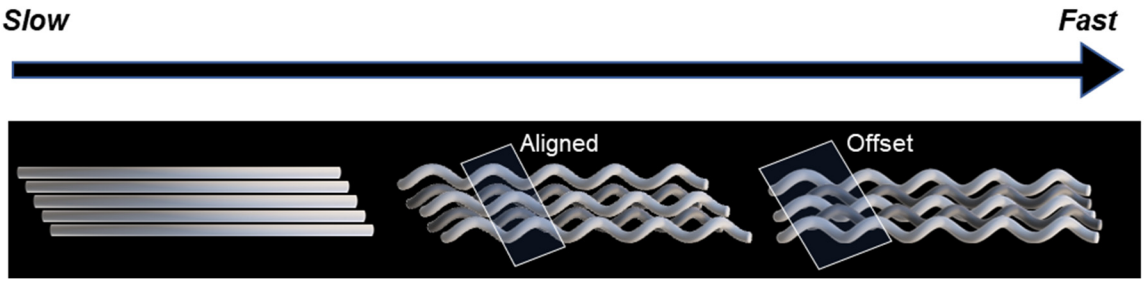

Supplementary Fig. 24. Schematic illustrating the tunability of the patterning through changing the evaporation rate.

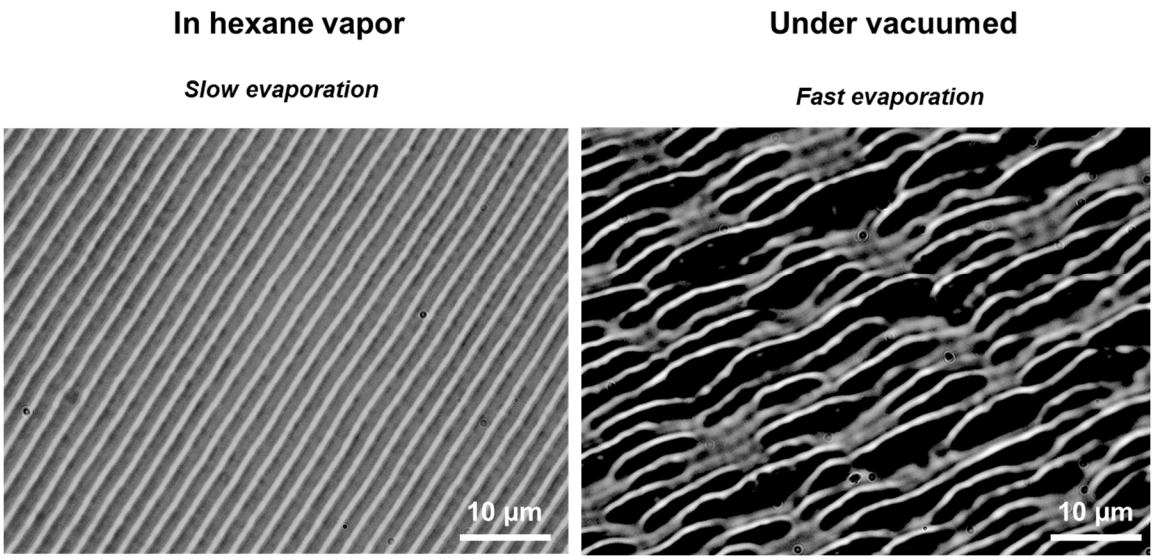

Supplementary Fig. 25. Optical microscope images for the thin films prepared through solvent evaporation of MSC solution with different evaporation rates. It shows by applying hexane vapor to slow down the evaporation rate (~0.003 μm/s), the as-formed thin film exhibits almost identical pattern as that obtained at the evaporation rate of 0.06 μm/s, while fast evaporation rate by applying a controlled vacuum condition results in wave-like thin film.

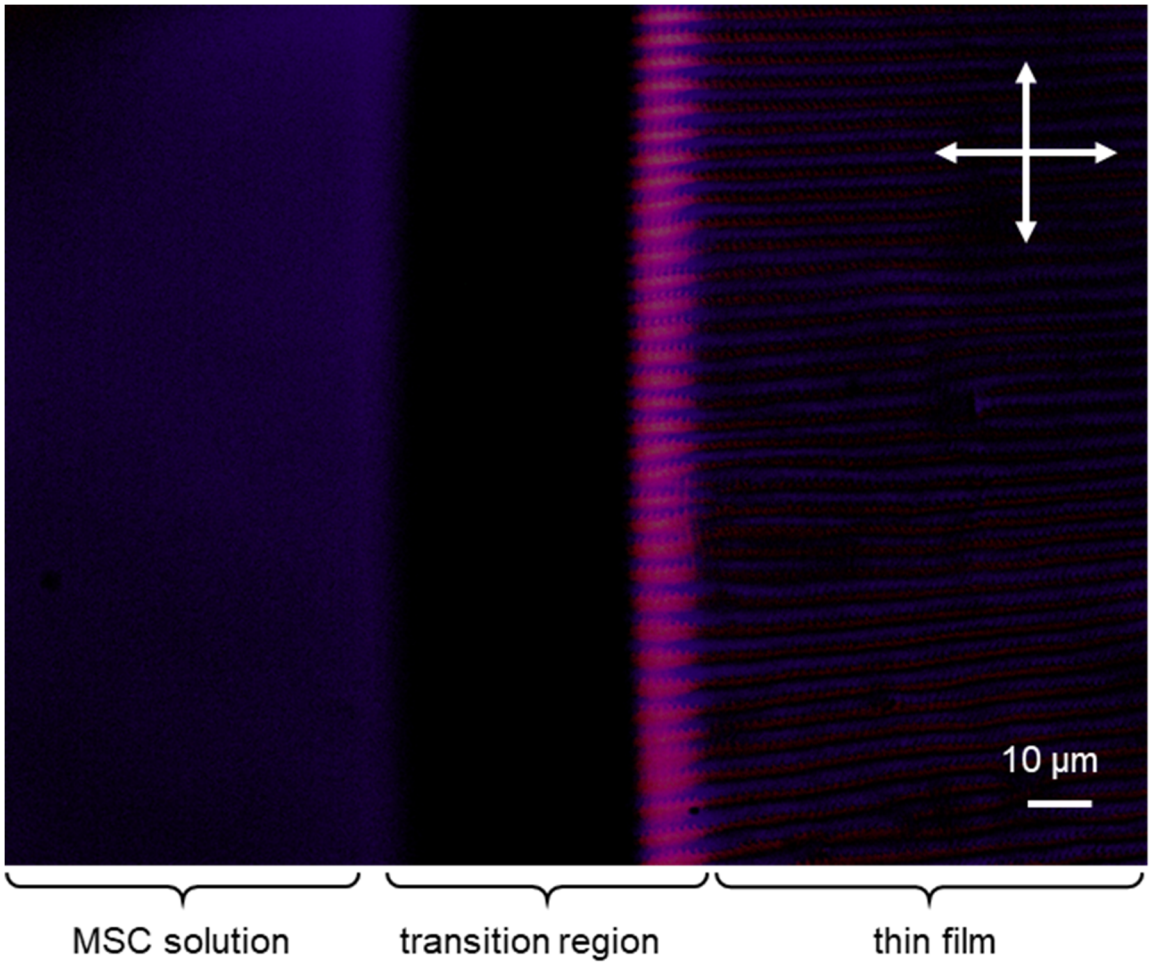

Supplementary Fig. 26. In-situ polarizing optical microscope image for the formation of highly aligned thin film upon solvent evaporation from 20 mg/mL MSC solution. Arbitrary colors are used here to clearly show the thin film formation. Under polarizing microscope, the MSC solution displays weak birefringence. During the solvent evaporation process, the drying front represents a region with high concentration contrast which make it opaque to the crossed polarized lights. The as-formed dry thin film contains fibers orientating perpendicularly to the evaporation front. Zoomed in OM analysis shows the constituent bands still orientate parallel to the drying front in **Supplementary Fig. 27**.

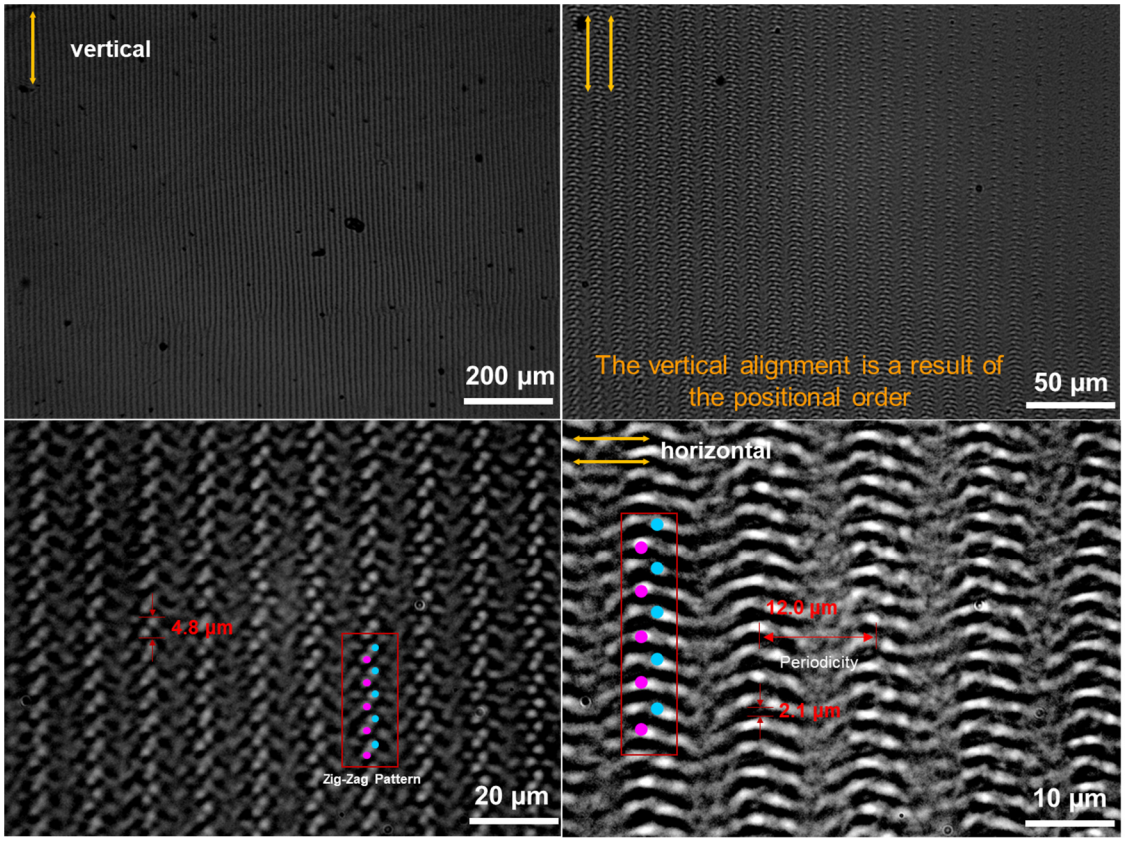

Supplementary Fig. 27. Optical microscope images for the thin films prepared through solvent evaporation of MSC solution with the evaporation rate of 0.6 μm/s. It shows that in a large viewing field, the thin film displays a vertical alignment, whereas the fibers actually align horizontally when viewing in a small viewing field.

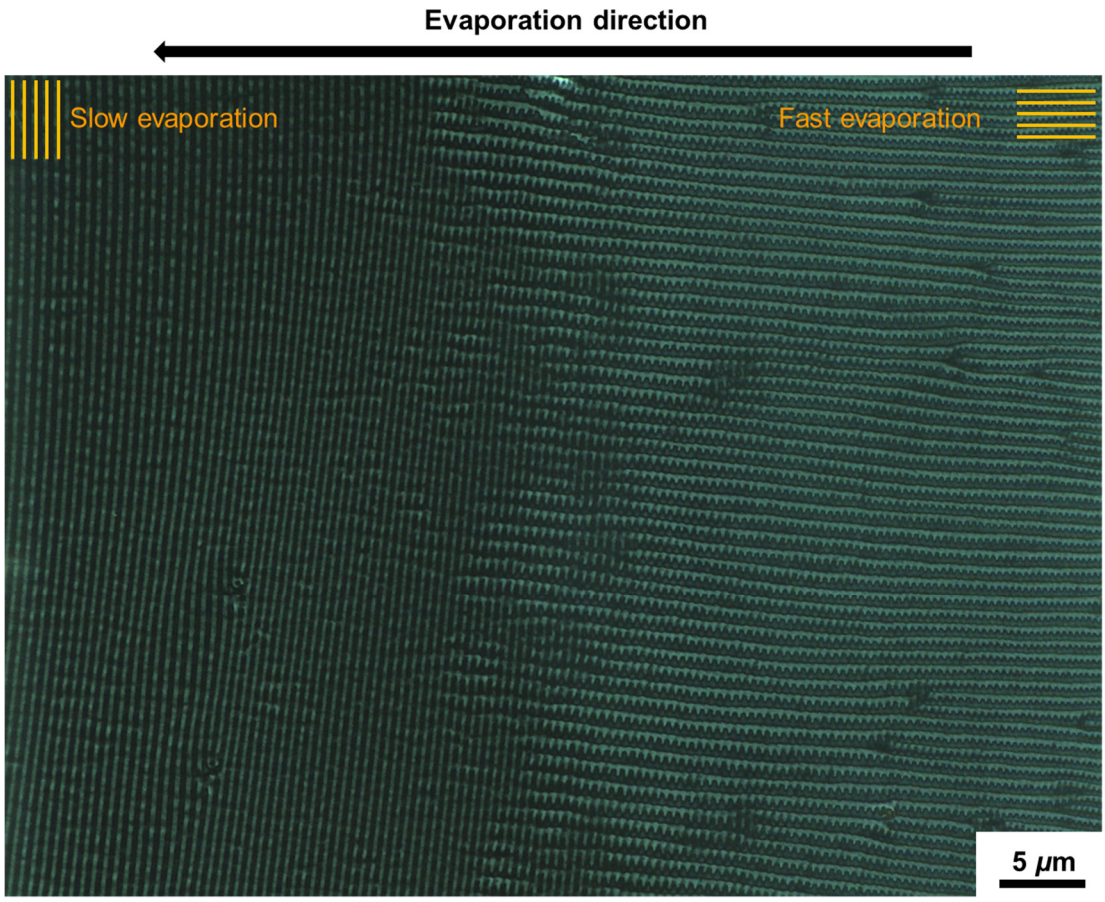

Supplementary Fig. 28. Optical microscope image for the thin film prepared through solvent evaporation of MSC solution with different evaporation rates. The evaporation front moves from left to right sides. At the beginning, the evaporation rate is relatively fast, which leads to the perpendicular alignment of the surface texture to the evaporation front. With the drying process going on, the as-formed dry thin film can slow down the evaporation of the hexane, eventually changing the patterning of the surface texture parallel to the evaporation front.

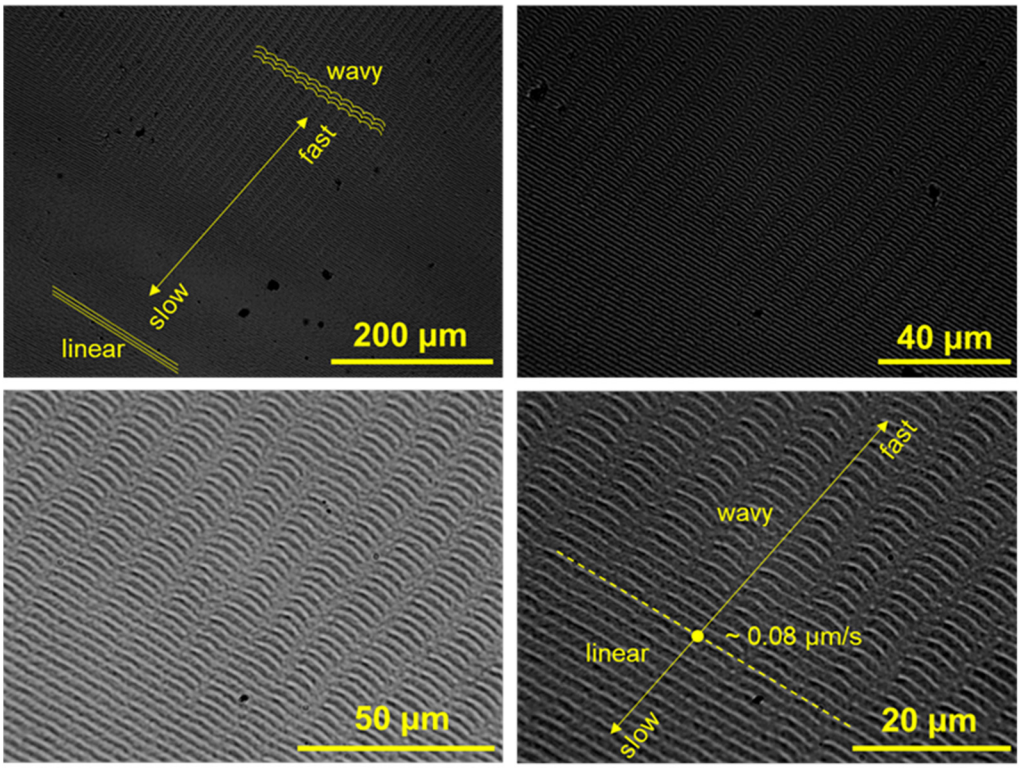

Supplementary Fig. 29. Optical images of the thin film prepared with an in-situ varied evaporate rate. As seen in the higher magnification images at bottom, relatively slow evaporation rates yield linearly aligned bands with one-dimensional periodicity, while a faster evaporation rate results in additional wave-like features, creating two-dimensional periodicity. (lower right) Optical image with added lines to demarcate the boundary between the two different periodic structures resulting from slow and fast evaporation rates.

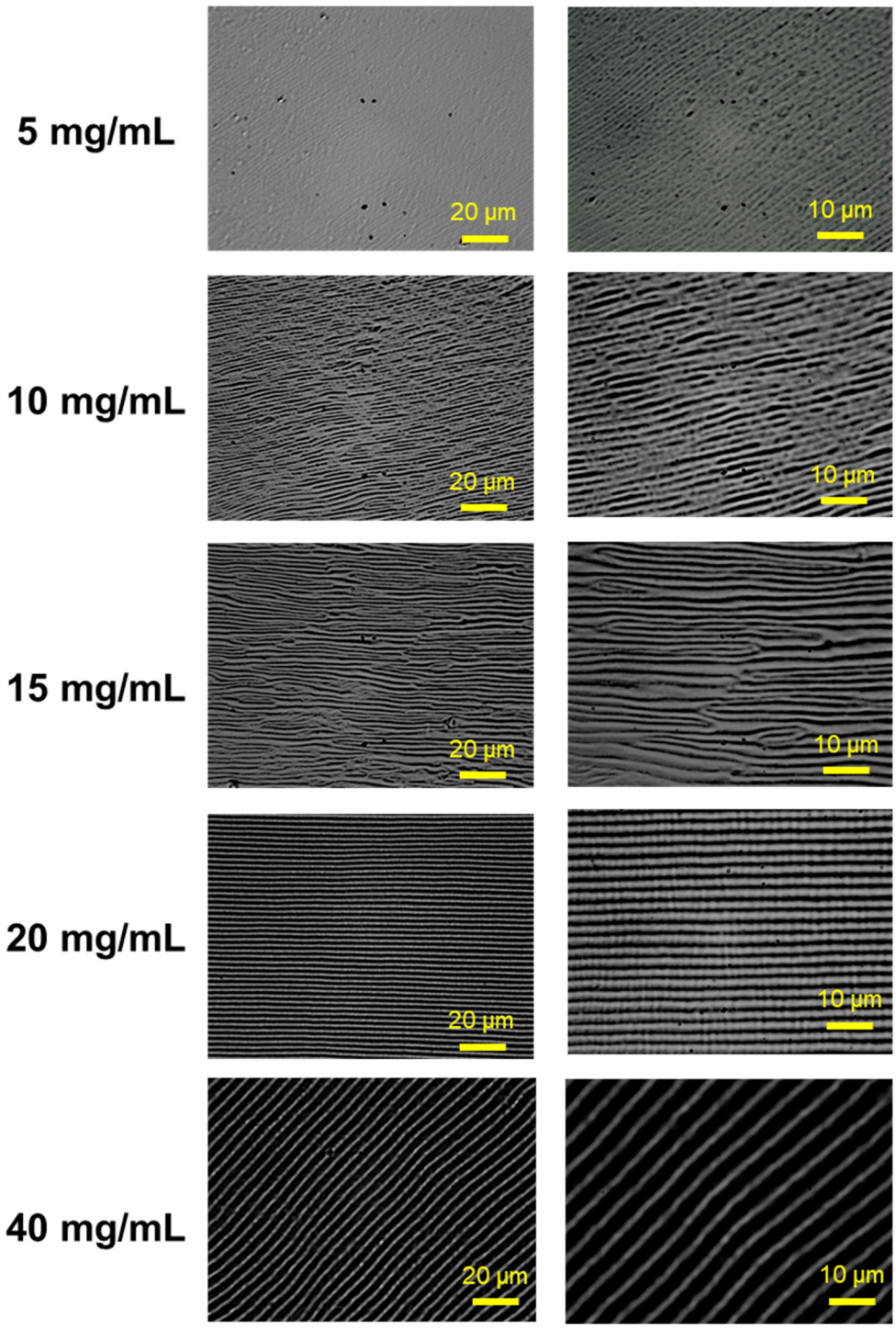

Supplementary Fig. 30. Optical microscope images for the thin films prepared from MSC solutions with different concentrations.

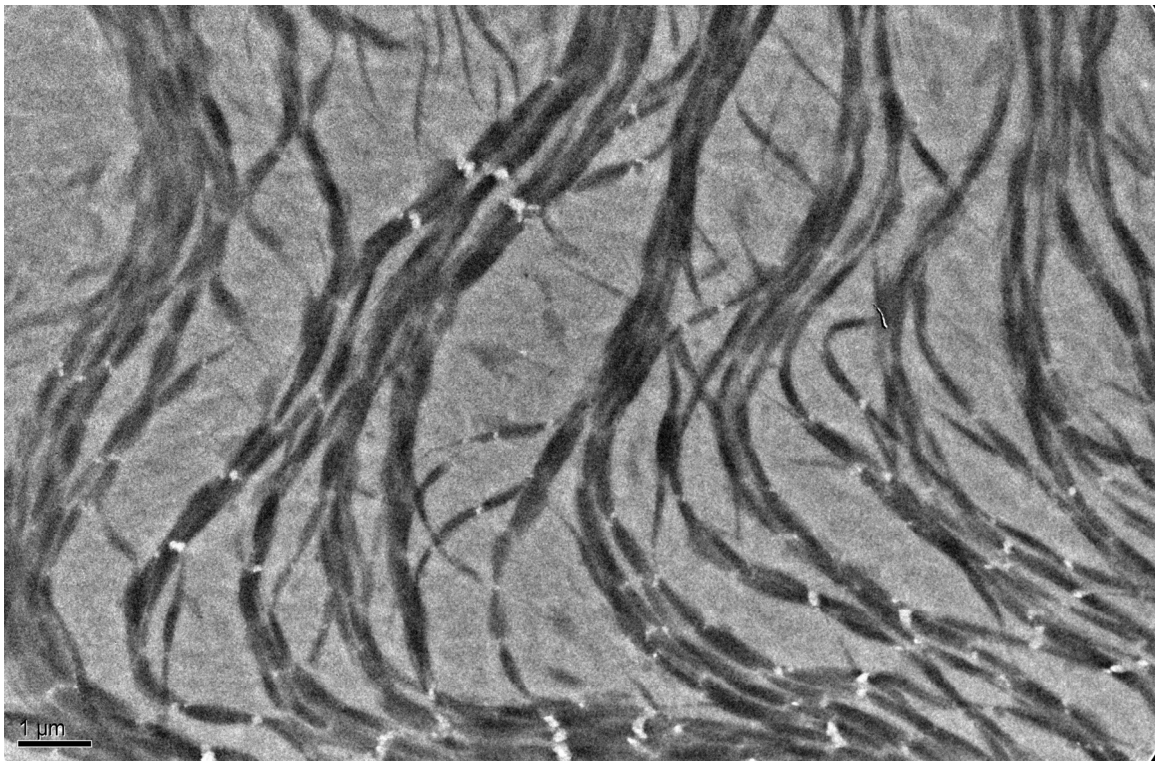

Supplementary Fig. 31. TEM images of the MSC filaments prepared by deposition of 1 mg/mL MSC solution in a copper TEM grid.

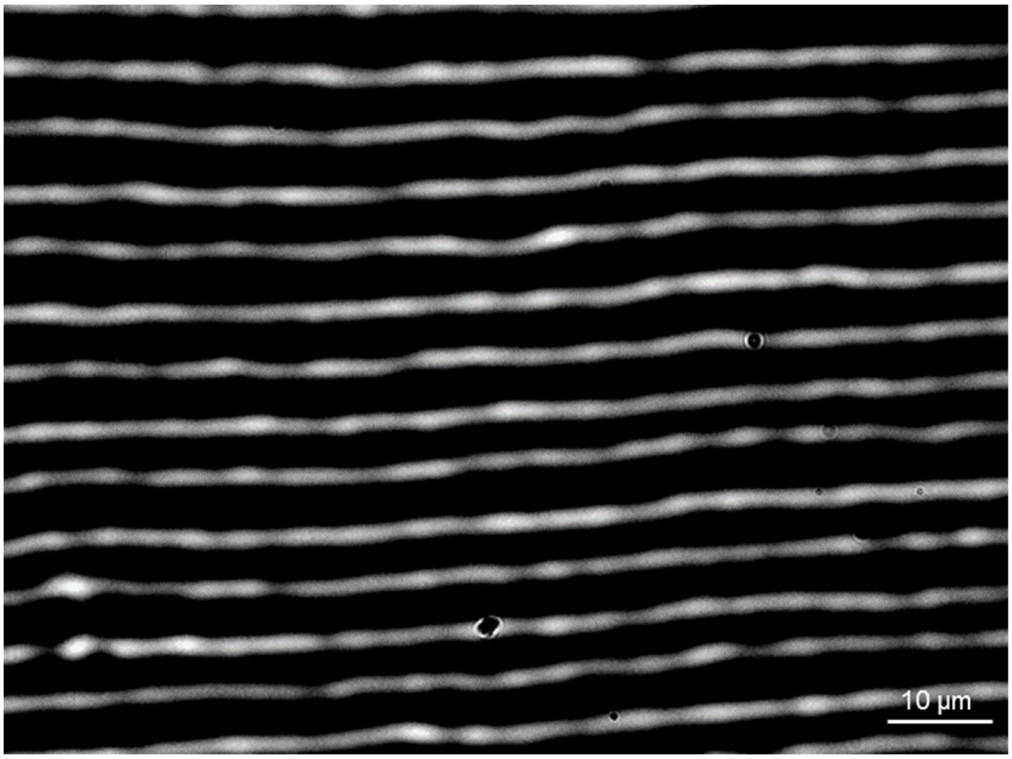

Supplementary Fig. 32. Optical microscope image of the thin film prepared from 40 mg/mL MSC solution. Note: image contrast is adjusted to clearly show the helical twisting nature of the fibers.

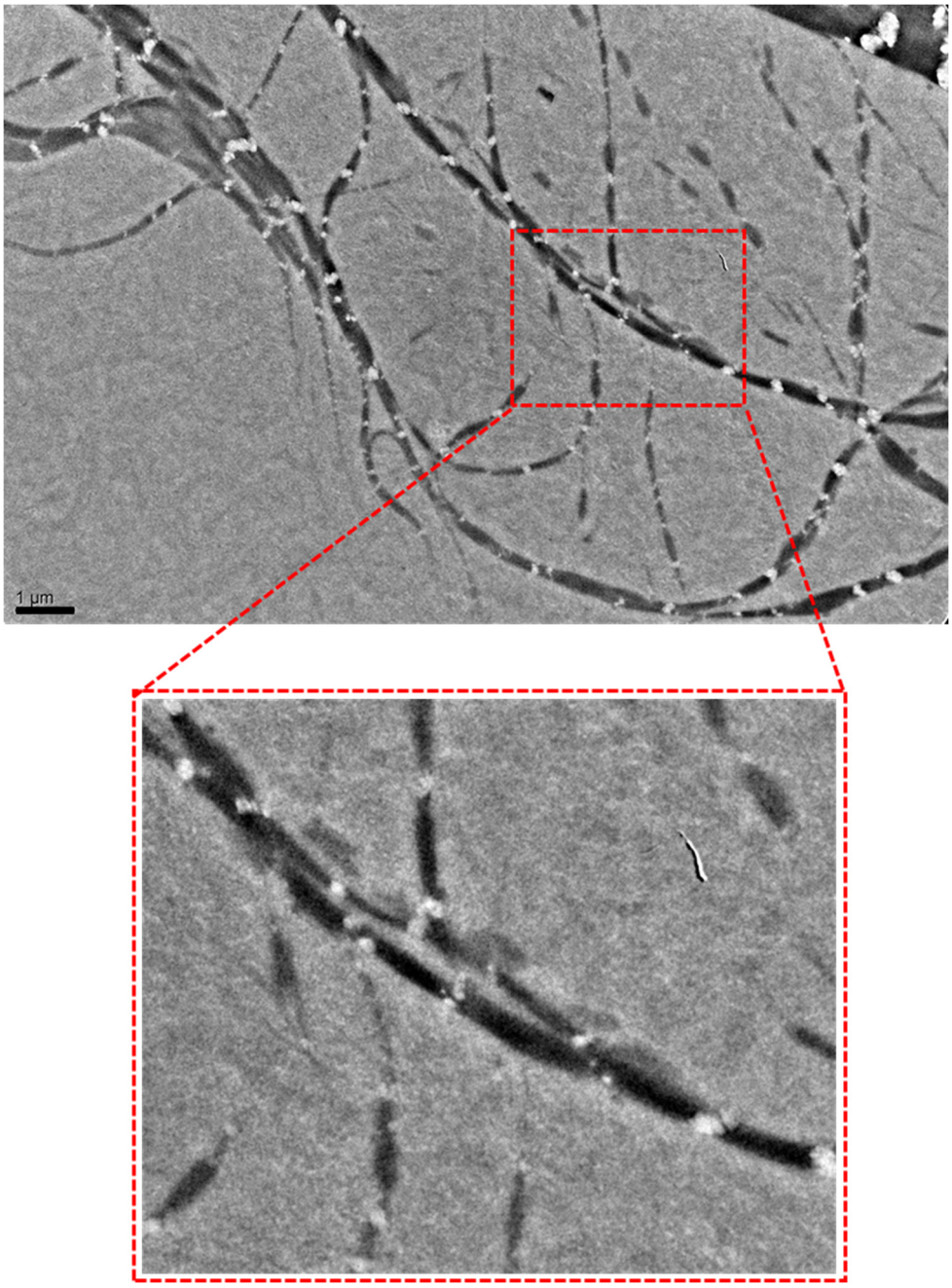

Supplementary Fig. 33. TEM images of the filaments obtained by sonicating 1 mg/mL MSC solution for 10 minutes.

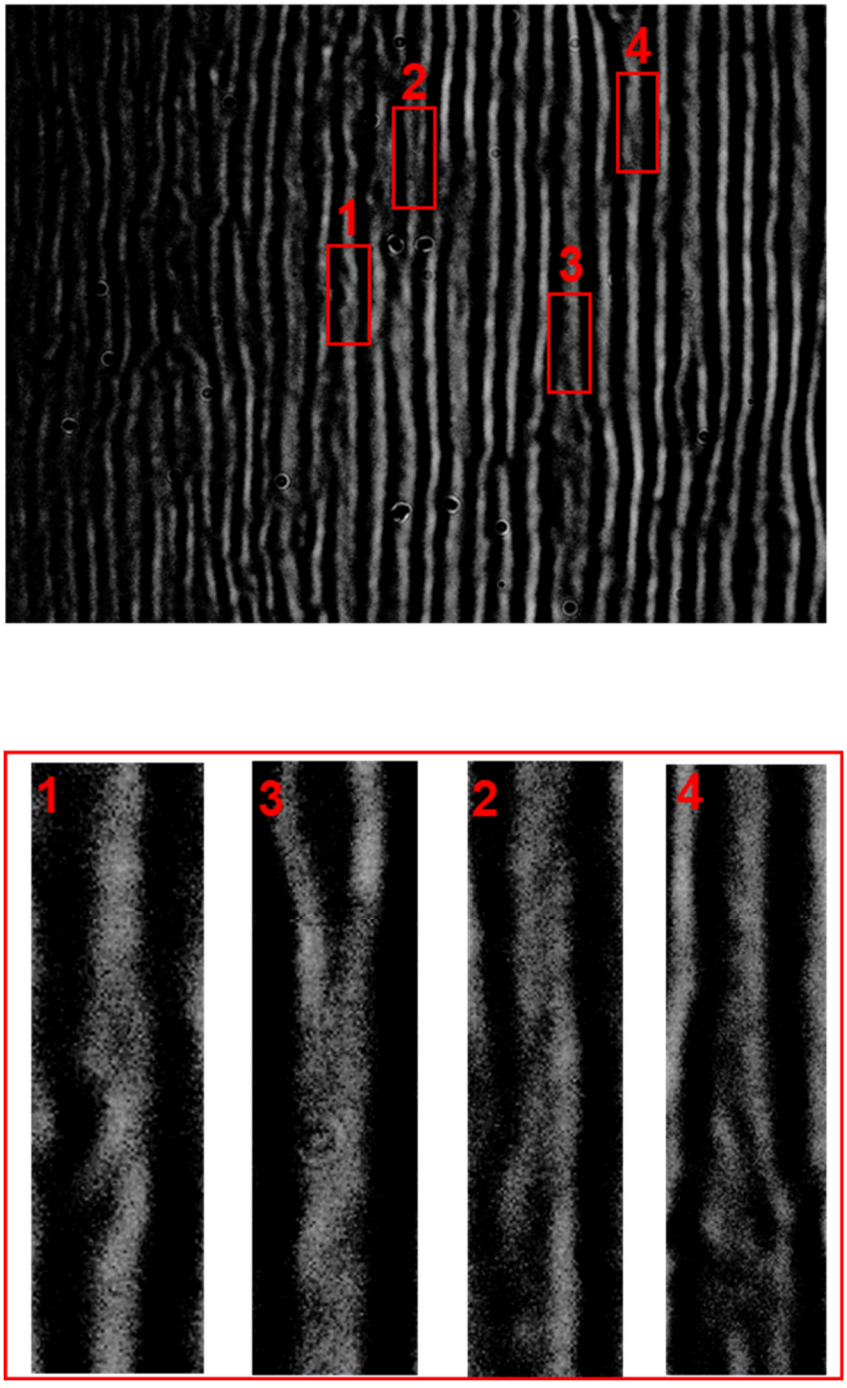

Supplementary Fig. 34. Optical microscope images taken by immersing thin film prepared from 20 mg/mL MSC solution into the hexane for several seconds. It indicates the fibers are disentangled into two sub-level fibers twisting around with each other. Note: arbitrary color is used to clearly show the structures.

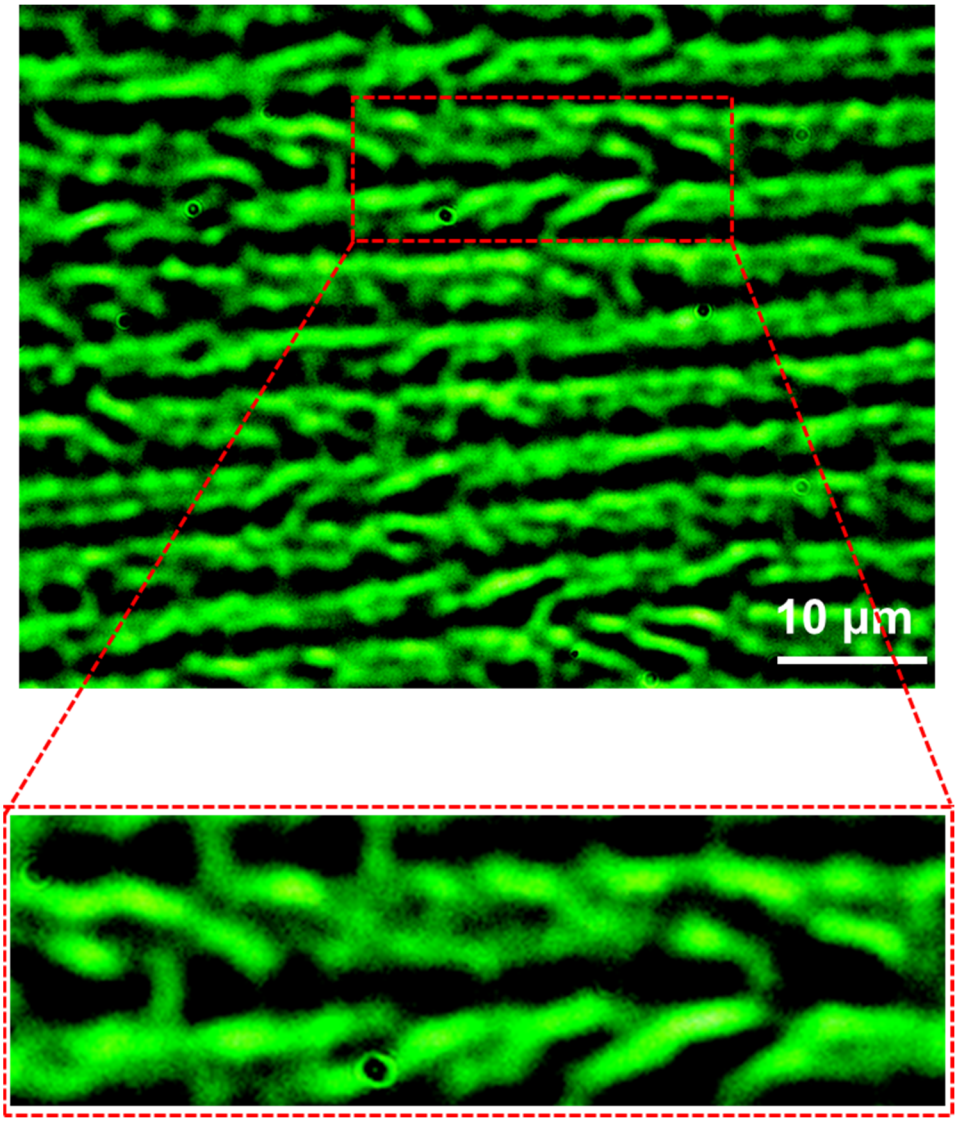

Supplementary Fig. 35. Optical microscope images taken by immersing thin film prepared from 40 mg/mL MSC solution into the hexane for several seconds. It indicates the fibers are disentangled into two sub-level fibers twisting around with each other. Note: arbitrary color is used to clearly show the structures.

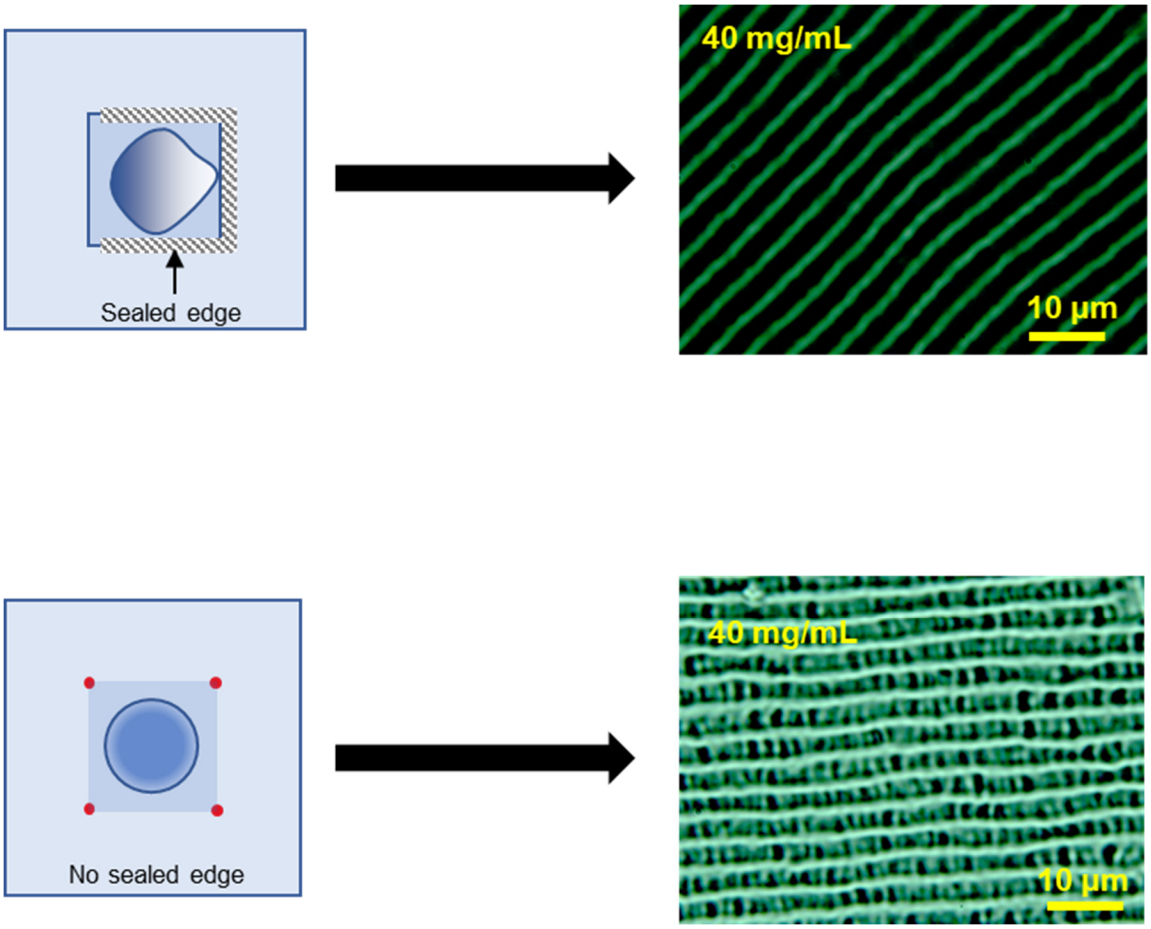

Supplementary Fig. 36. Thin films prepared from 40 mg/mL MSC solution by applying different evaporation confinement. (top) Linear patterns from three-side confinement. (bottom) By controlling the evaporation direction front of a 40 mg/mL solution to be radial results in a thin film composed of two layers of straight fibers, which are perpendicular to each other. Arbitrary color is used in the optical microscope images.

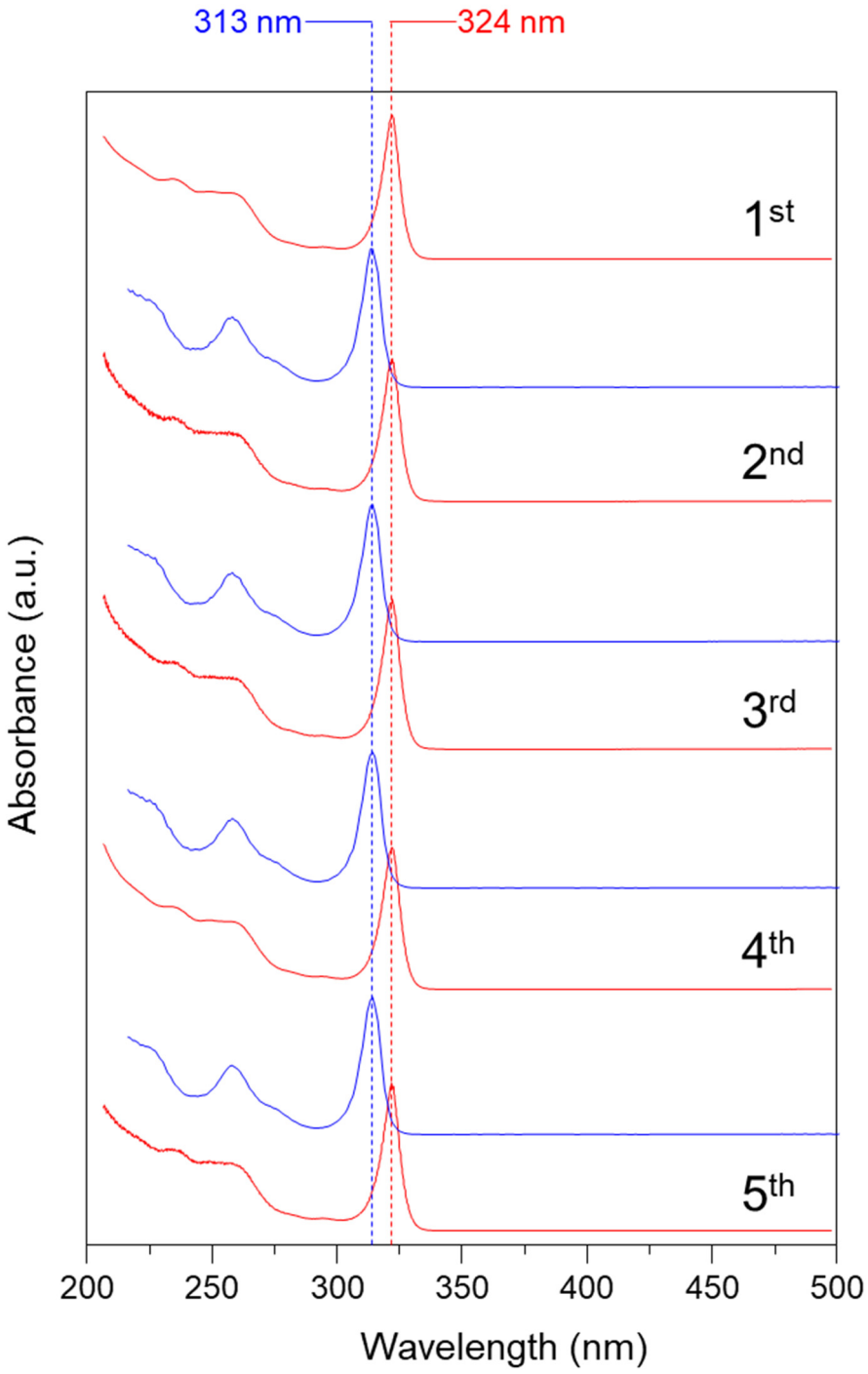

Supplementary Fig. 37. Absorption spectra of the thin film de/adsorption of methanol molecules for five rounds. It shows the pristine thin film has a characteristic absorption peak at 324 nm and after methanol treatment, the absorption peak shifts to 313 nm. The desorption of methanol molecules by gentle heating for 30 min can bring the absorption peak back to 324 nm again. Such conversion can be recycled for at least 5 times.

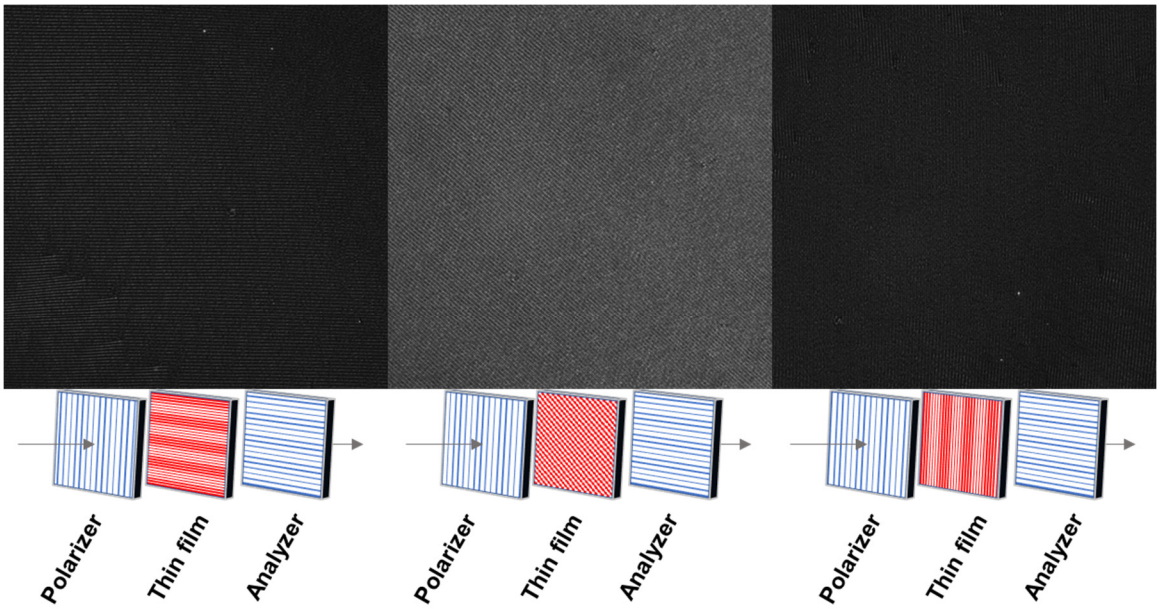

Supplementary Fig. 38. Polarizing optical microscope images for the thin film. The polarizer and analyzer are perpendicular to each other. By rotating the sample stage, the alignment of the thin film can be set to have angles of 0° (left), 45° (middle) and 90° (right) to the polarizer (or analyzer). The highest intensity of the transmitting light appears when the thin film has a 45° angle to the polarizer (or analyzer).

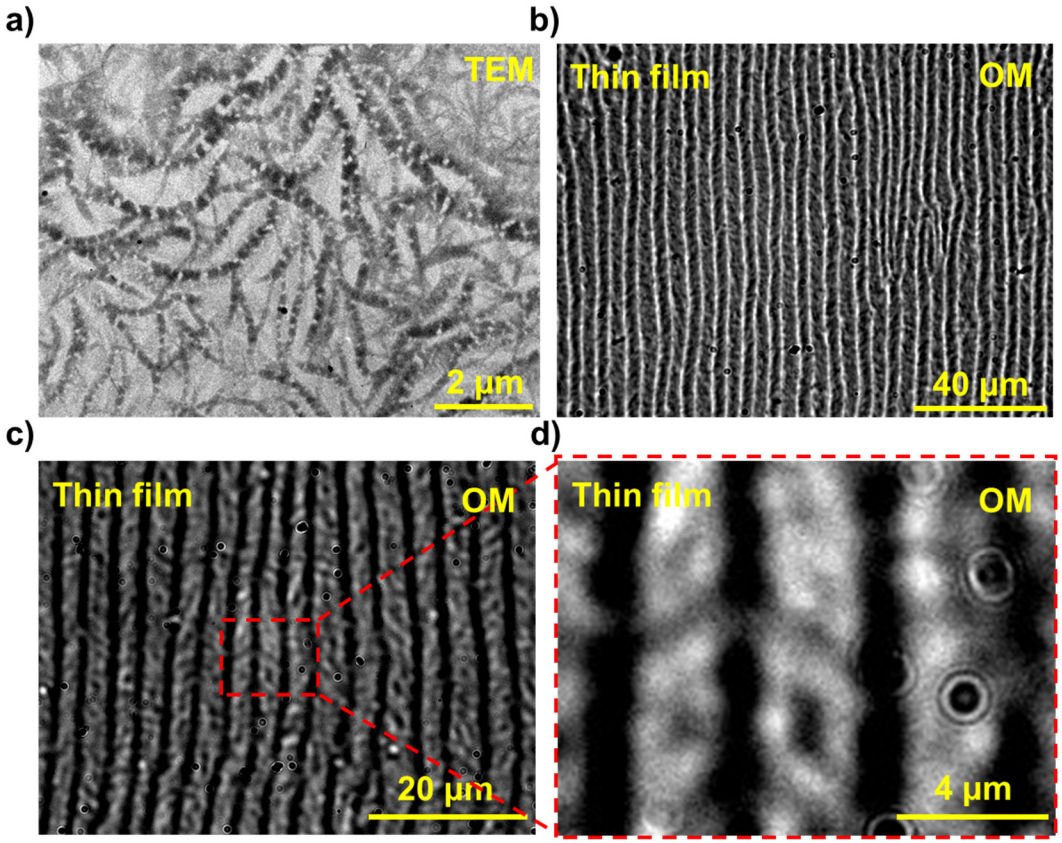

Supplementary Fig. 39. Hierarchical self-assembly of CdO nanoclusters. (a) TEM image of the filament structure made up with CdO nanoclusters. (b-d) Optical images for the thin film prepared from 20 mg/mL CdO nanocluster solution in hexane through solvent evaporation.

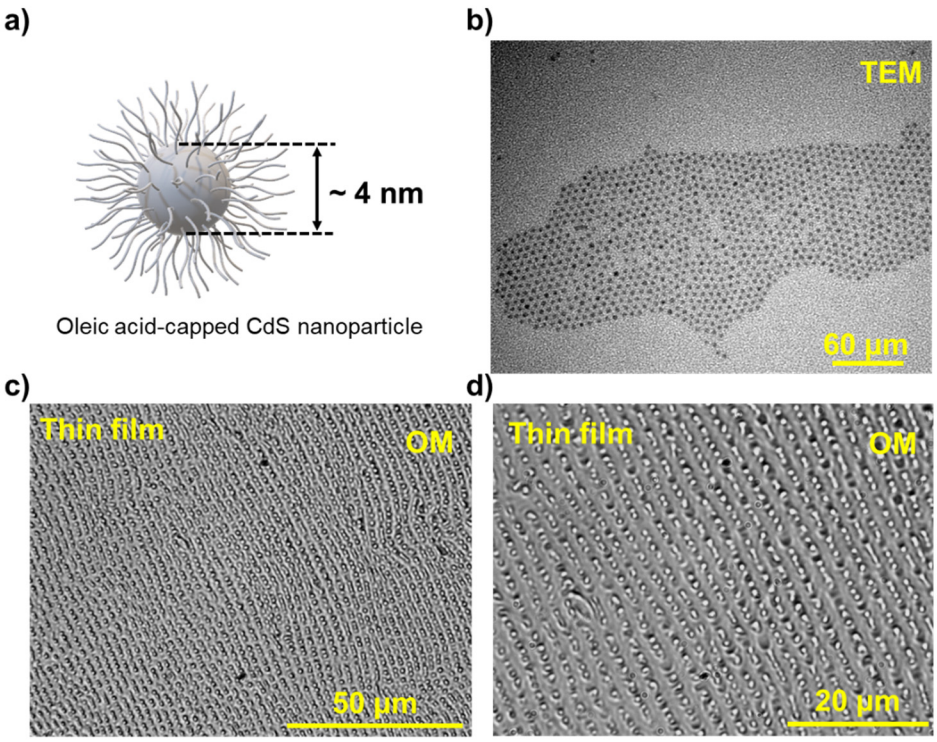

Supplementary Fig. 40. Self-assembly of larger CdS nanoparticles. (a) Schematic illustration of a 4 nm CdS nanoparticles capped with oleic acid. (b) TEM image of the as-prepared 4 nm CdS nanoparticles. (c) and (d) Optical images of the thin film prepared from 4 nm CdS nanoparticles through the solvent evaporation process.

2. Supplementary table

Supplementary Table 1 Preparation conditions for the thin films investigated in current work

Concentration	Evaporation geometry	Evaporation rate	Band spacing	Correspondence to figure in current work
5 mg/mL	Linear	N. E.	∽ 0.8 μm	Fig. S30 (1st row)
10 mg/mL	Linear	N. E.	∽ 1.2 μm	Fig. S30 (2nd row)
15 mg/mL	Linear	N. E.	∽ 1.5 μm	Fig. S30 (3rd row)
20 mg/mL	Linear	∽ 0.06 μm/s[a]	∽ 2.0 μm[d]	Fig. 1A,B,C (left), Fig. 2C,D, Fig. 3A-F, Fig. 4A, Fig. 5, Fig. S8,S9, Fig. S14-S17, S21, S23, Fig. S30 (4th row), Fig. S38
20 mg/mL	Linear	∽ 0.03 μm/s[b]	∽ 2.0 μm	Fig. S25 (left)
20 mg/mL	Radical	∽ 0.06 μm/s[a]	∽ 2.0 μm	Fig. 2E,F, Fig. S18-S20
20 mg/mL	Linear	∽ 0.1 μm/s[c]	∽ 2.0 μm	Fig. 4B
20 mg/mL	Linear	∽ 0.6 μm/s[c]	∽ 2.0 μm	Fig. 4C, Fig. S26,S27
20 mg/mL	Linear	Fast[c]	e	Fig. S25 (right)
20 mg/mL	Radom	N. E.	e	Fig. 1C (right), Fig. 2G,H, Fig. S22
40 mg/mL	Linear	N. E.	∽ 5.0 μm	Fig. 4E (3rd from left), Fig. S30 (5th row), Fig. S32, Fig. S36 (top)
40 mg/mL	Radical	N. E.	∽ 5.0 μm	Fig. S36 (bottom)
100 mg/mL	Linear	N. E.	e	Fig. 4F

Notes:
Linear = Two-glass configuration with three edges sealed (see Fig. 2C in main text).
Radical = Two-glass configuration with four edges opened (see Fig. 2E in main text).
Radom = One-glass configuration without the covering glass slide (see Fig. 2G in main text).
N.E. = Natural evaporation.
Fast = Evaporation takes place fast and accurate measurement of the evaporation rate cannot be made.
a = Solvent evaporation takes place naturally.
b = Solvent evaporation takes place in a hexane vapor atmosphere.

c = Solvent evaporation takes place under controlled vacuum condition.
d = The band spacing was measured out based on the optical microscope images. Only this thin film was measured for thickness.
e = The band spacing cannot be accurately measured out due to the complex band patterning. The corresponding figures can be found in appropriate positions in the main texts and supplementary information file.
The gap between the two glass slides were kept in about 100 μm for all experiments.

3. References

1. Mendelson, K. S.; Karioris, F. G., Multislit Diffraction Patterns Using a Slit-Grating Combination. *Am. J. Phys.* **1995,** *63* (1), 53-56.
2. Berreman, D. W., Optics in Smoothly Varying Anisotropic Planar Structures: Application to Liquid-Crystal Twist Cells*. *J. Opt. Soc. Am.* **1973,** *63* (11), 1374-1380.
3. Frank L. Pedrotti, L. S. P., Leno M. Pedrott, *Introduction to Optics (3rd Edition)*. Cambridge University Press: 2006.
4. Rumsey, V., Some New Forms of Huygens' Principle. *IRE Trans. Antennas Propag.* **1959,** *7* (5), 103-116.
5. Kettler, J. E., The compact disk as a diffraction grating. *Am. J. Phys.* **1991,** *59* (4), 367-368.
6. Resnick, J.; Monroy-Ramírez, F. A., Teaching the concept of dispersion by diffraction of light to elementary school students. SPIE: 2017; Vol. 10452, pp 707-712.
7. Tang, Z.; Kotov Nicholas, A.; Giersig, M., Spontaneous Organization of Single CdTe Nanoparticles into Luminescent Nanowires. *Science* **2002,** *297* (5579), 237-240.
8. Atkins, P. W. D. P. J., *Atkins' Physical chemistry*. Oxford University Press: Oxford; New York, 2006.
9. Williamson Curtis, B.; Nevers Douglas, R.; Nelson, A.; Hadar, I.; Banin, U.; Hanrath, T.; Robinson Richard, D., Chemically Reversible Isomerization of Inorganic Clusters. *Science* **2019,** *363* (6428), 731-735.
10. Luedtke, W. D.; Landman, U., Structure, Dynamics, and Thermodynamics of Passivated Gold Nanocrystallites and Their Assemblies. *J. Phys. Chem.* **1996,** *100* (32), 13323-13329.
11. Frederick, M. T.; Achtyl, J. L.; Knowles, K. E.; Weiss, E. A.; Geiger, F. M., Surface-Amplified Ligand Disorder in CdSe Quantum Dots Determined by Electron and Coherent Vibrational Spectroscopies. *J. Am. Chem. Soc.* **2011,** *133* (19), 7476-7481.
12. Akcora, P.; Liu, H.; Kumar, S. K.; Moll, J.; Li, Y.; Benicewicz, B. C.; Schadler, L. S.; Acehan, D.; Panagiotopoulos, A. Z.; Pryamitsyn, V.; Ganesan, V.; Ilavsky, J.; Thiyagarajan, P.; Colby, R. H.; Douglas, J. F., Anisotropic Self-Assembly of Spherical Polymer-Grafted Nanoparticles. *Nat. Mater.* **2009,** *8* (4), 354-359.
13. Singh, G.; Chan, H.; Baskin, A.; Gelman, E.; Repnin, N.; Král, P.; Klajn, R., Self-Assembly of Magnetite Nanocubes into Helical Superstructures. *Science* **2014,** *345* (6201), 1149-1153.
14. Viney, C.; Putnam, W. S., The banded microstructure of sheared liquid-crystalline polymers. *Polymer* **1995,** *36* (9), 1731-1741.
15. Liu, Y.-H.; Wang, F.; Wang, Y.; Gibbons, P. C.; Buhro, W. E., Lamellar Assembly of Cadmium Selenide Nanoclusters into Quantum Belts. *J. Am. Chem. Soc.* **2011,** *133* (42), 17005-17013.
16. Huang, J.; Fan, R.; Connor, S.; Yang, P., One-Step Patterning of Aligned Nanowire Arrays by Programmed Dip Coating. *Angew. Chem. Int. Ed.* **2007,** *46* (14), 2414-2417.
17. Vermant, J.; Moldenaers, P.; Mewis, J.; Picken, S. J., Band formation upon cessation of flow in liquid-crystalline polymers. *J. Rheol.* **1994,** *38* (5), 1571-1589.
18. Navard, P., Formation of band textures in hydroxypropylcellulose liquid crystals. *J. Polym. Sci., Part B: Polym. Phys.* **1986,** *24* (2), 435-442.

19. Fischer, H.; Keller, A.; Windle, A. H., The origin of banded textures induced by shear—a suggested scheme and a relevant rheological effect. *J. Non-Newton. Fluid Mech.* **1996,** *67*, 241-268.
20. Picken, S. J.; Moldenaers, P.; Berghmans, S.; Mewis, J., Experimental and theoretical analysis of band formation in polymeric liquid crystals upon cessation of flow. *Macromolecules* **1992,** *25* (18), 4759-4767.
21. Kiss, G.; Porter, R. S., Flow induced phenomena of lyotropic polymer liquid crystals: the negative normal force effect and bands perpendicular to shear. In *Mechanical and thermophysical properties of polymer liquid crystals*, Springer: 1998; pp 342-406.
22. Wang, J.; Labes, M. M., Control of the anisotropic mechanical properties of liquid crystal polymer films by variations in their banded texture. *Macromolecules* **1992,** *25* (21), 5790-5793.
23. Chung, W.-J.; Oh, J.-W.; Kwak, K.; Lee, B. Y.; Meyer, J.; Wang, E.; Hexemer, A.; Lee, S.-W., Biomimetic self-templating supramolecular structures. *Nature* **2011,** *478* (7369), 364-368.
24. Bodiguel, H.; Doumenc, F.; Guerrier, B., Stick−Slip Patterning at Low Capillary Numbers for an Evaporating Colloidal Suspension. *Langmuir* **2010,** *26* (13), 10758-10763.
25. Deegan, R. D.; Bakajin, O.; Dupont, T. F.; Huber, G.; Nagel, S. R.; Witten, T. A., Capillary Flow as the Cause of Ring Stains from Dried Liquid Drops. *Nature* **1997,** *389* (6653), 827-829.
26. Adachi, E.; Dimitrov, A. S.; Nagayama, K., Stripe Patterns Formed on a Glass Surface during Droplet Evaporation. *Langmuir* **1995,** *11* (4), 1057-1060.
27. Yabu, H.; Shimomura, M., Preparation of Self-Organized Mesoscale Polymer Patterns on a Solid Substrate: Continuous Pattern Formation from a Receding Meniscus. *Adv. Funct. Mater.* **2005,** *15* (4), 575-581.
28. Grason, G. M.; Bruinsma, R. F., Chirality and Equilibrium Biopolymer Bundles. *Phys. Rev. Lett.* **2007,** *99* (9), 098101.
29. Grason, G. M., Braided bundles and compact coils: The structure and thermodynamics of hexagonally packed chiral filament assemblies. *Phys. Rev. E* **2009,** *79* (4), 041919.
30. Kleis, J.; Schröder, E., Van der Waals Interaction of Simple, Parallel Polymers. *J. Chem. Phys.* **2005,** *122* (16), 164902.
31. Williamson, C. B.; Nevers, D. R.; Nelson, A.; Hadar, I.; Banin, U.; Hanrath, T.; Robinson, R. D., Chemically Reversible Isomerization of Inorganic Clusters. *Science* **2019,** *363* (6428), 731.
32. Nevers, D. R.; Williamson, C. B.; Savitzky, B. H.; Hadar, I.; Banin, U.; Kourkoutis, L. F.; Hanrath, T.; Robinson, R. D., Mesophase Formation Stabilizes High-Purity Magic-Sized Clusters. *J. Am. Chem. Soc.* **2018,** *140* (10), 3652-3662.
33. Guerrero-Martínez, A.; Alonso-Gómez, J. L.; Auguié, B.; Cid, M. M.; Liz-Marzán, L. M., From Individual to Collective Chirality in Metal Nanoparticles. *Nano Today* **2011,** *6* (4), 381-400.
34. Nakano, T.; Pietropaolo, A.; Kamata, M., Chirality Analysis of Helical Polymers. *Chemistry Teacher International* **2021,** *3* (1), 67-76.
35. Morrow, S. M.; Bissette, A. J.; Fletcher, S. P., Transmission of Chirality Through Space and Across Length Scales. *Nat. Nanotechnol.* **2017,** *12* (5), 410-419.

36. Korgel, B. A.; Fitzmaurice, D., Small-Angle X-Ray-Scattering Study of Silver-Nanocrystal Disorder-Order Phase Transitions. *Phys. Rev. B* **1999,** *59* (22), 14191.
37. Jing, G.; Bodiguel, H.; Doumenc, F.; Sultan, E.; Guerrier, B., Drying of Colloidal Suspensions and Polymer Solutions near the Contact Line: Deposit Thickness at Low Capillary Number. *Langmuir* **2010,** *26* (4), 2288-2293.